Phonon focusing in cubic crystals

D. C. Hurley and J. P. Wolfe
Physics Department and Materials Research Laboratory, University of Illinois at Urbana–Champaign, Urbana, Illinois 61801
(Received 25 January 1985)

The nature of the phonon intensity pattern associated with low-temperature heat-pulse propagation is examined theoretically for a wide range of cubic crystals. In general, huge anisotropies in the thermal flux are predicted due to phonon focusing. The phonon-focusing patterns of cubic crystals divide naturally into two major groups, as distinguished by the sign of their anisotropy factor $\Delta = C_{11}/C_{44} - C_{12}/C_{44} - 2$. Experimental and theoretical intensity patterns of CaF_2 and Si in the long-wavelength, dispersionless limit are examined in detail to illustrate the typical focusing-pattern features characteristic of positive and negative Δ. For both regimes, the evolution of particular pattern structures is studied systematically as the elastic constants are varied. Investigation of the flux-intensity pattern and slowness-surface topology for various elastic constants reveals distinct trends in the phonon-focusing structures. Based on this study, we have defined a small number of angular dimensions (one or two for each phonon mode and anisotropy regime) which quantitatively determine the principal directions of singular flux. The variations of these angles are mapped onto the general elastic-parameter space. We thus present a means for quickly determining the angular positions of the principle phonon-focusing caustics for an arbitrary set of elastic constants.

I. INTRODUCTION

At low temperatures, the ballistic heat flux emitted from a point source in a crystal is strongly concentrated along certain crystalline directions—an effect known as "phonon focusing."[1–3] The nature and degree of angular anisotropy that is present in the crystal's heat-flux intensity pattern are directly determined by the elastic constants of the crystal. Phonon-imaging experiments have examined these pronounced anisotropies in order to extract information about the propagation and scattering of high-frequency acoustic phonons. In Ge, a knowledge of phonon focusing was required to characterize the interaction of phonons with electronic states.[4–8] Phonon scattering from dislocations in LiF (Ref. 9) and the effect of piezoelectricity on ballistic heat flow in $LiNbO_3$ (Ref. 10) were more clearly understood by examining the flux-intensity patterns for these crystals. A detailed understanding of phonon focusing has proved essential in the characterization of large **k** vector phonons in Ge (Refs. 11 and 12) and GaAs (Refs. 13 and 14). In each of these cases, a specific, unique intensity pattern was involved.

In this paper we present a systematic study of the nondispersive phonon-focusing patterns of cubic crystals in general. A previous systematic study of phonon focusing in cubic crystals was reported by Every,[15] who emphasized the aspects of singular flux patterns as a physical application of catastrophe theory. Also, Armbruster and Dangelmayr[16] have examined the general topological features of phonon focusing. With the advent of more advanced computing techniques—Monte Carlo flux-intensity simulations and three-dimensional representations of phonon wave surfaces—it is now possible to examine the relative intensities and origins of the intricate focusing patterns in more detail. We show the evolution of focusing patterns over a wide range of elastic constants. In addition to revealing topological details, this generalized summary may serve as a practical reference for characterizing the heat-flux anisotropy in a particular crystal without having to resort to a detailed calculation.

II. BACKGROUND AND METHODS

Wave propagation in a continuous, anisotropic medium has been studied for many years.[17,18] The equations of continuum elasticity theory which govern the propagation of lattice waves (i.e., phonons in the long-wavelength, dispersionless limit) in crystals are dependent on the crystal density ρ and the elastic constants C_{IJ} (the nonzero elements of the elastic stiffness tensor C_{ijlm}).[19] For crystals with cubic symmetry, there are only three elastic constants: C_{11}, C_{12}, and C_{44}. This means that phonon propagation, and thus ultimately phonon-focusing patterns, can be treated as a function of two variables, generally taken as the ratios $a = C_{11}/C_{44}$ and $b = C_{12}/C_{44}$. (The magnitudes of the C_{IJ} and ρ determine the absolute velocities, but the ratios a and b completely determine the anisotropy in velocity.) All cubic crystals can thus be mapped into a two-dimensional "elastic-parameter space."[1,15] The position of several different materials as plotted in this space is shown in Fig. 1.[20]

For certain hypothetical values of elastic constants, there is no anisotropy in phonon velocity. This condition for elastic isotropy,[19] $C_{11} - C_{12} - 2C_{44} = 0$, appears now as the line $\Delta \equiv a - b - 2 = 0$, as shown in Fig. 1. All real, anisotropic crystals fall on either side of this isotropy line. The line serves as a natural boundary with which to divide crystals into two distinct groups: those for which $\Delta > 0$ ("positive-Δ regime") above the isotropy line, and those with $\Delta < 0$ ("negative-Δ regime") below the isotropy line.

Restrictions exist on the values of a and b possible for real crystals (as discussed in detail in Ref. 21). For $a < b$ and $a < -2b$, thermodynamic constraints on the C_{IJ} are not met. In addition, for $a < 1$ and $b < -1$, the acoustic transverse phase velocity exceeds the longitudinal phase velocity for certain crystalline directions, which is extremely rare.[15] The net result is that consideration of elastic-parameter space can be confined to the upper region bordered by the thick lines in Fig. 1.

This classification of crystalline properties makes it possible to study the phonon-focusing patterns of cubic crystals in a systematic manner. Each different combination of the elastic ratios a and b will produce a unique focusing pattern, even if no actual material exists with those ratios. By treating a and b as continuous variables and noting the relationships between the intensity patterns for different pairs of ratios, the similarities between focusing patterns in different crystals can be understood. Also, in this way trends can be found in the flux-intensity patterns. Knowing these trends, it is possible to make rapid, quantitative predictions about the phonon-focusing pattern for any material, without the need for specific, detailed calculations.

Examples of the phonon-intensity pattern for positive- and negative-Δ crystals are shown in Figs. 2(a) and 2(b), which are experimental images of CaF_2 and Si, respectively. These images were taken using the phonon-imaging technique developed by Northrop and Wolfe.[3] Bright areas represent the ballistic heat flux emitted from a point source (laser spot) which is scanned across a particular surface of the crystal. For the CaF_2 crystal, the scanned surface is (111); for the Si crystal, it is (100). The heat flux is detected by a fixed bolometer on the opposite surface. The images were recorded with broad time gates so that both transverse phonon modes were included. Such images show that positive-Δ materials such as CaF_2 display complex structures near the $\langle 111 \rangle$ crystalline direction, while negative-Δ materials such as Si exhibit complex structures around the $\langle 100 \rangle$ and $\langle 111 \rangle$ crystalline directions.

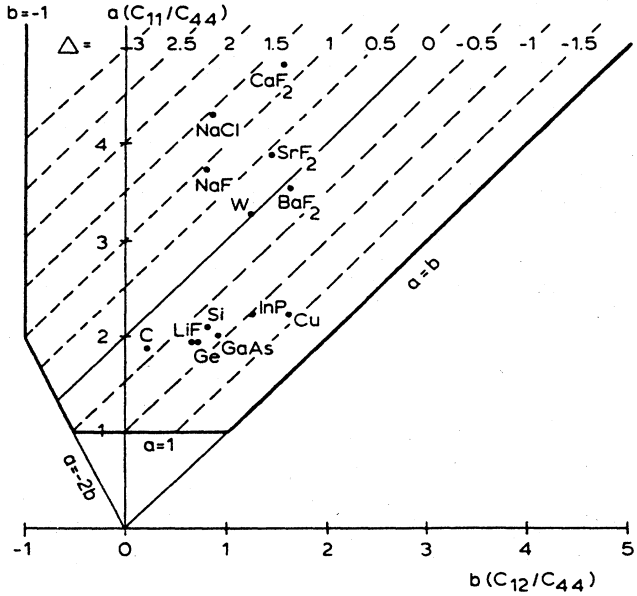

FIG. 1. Elastic-parameter space for cubic crystals. Materials are plotted according to the elastic ratios $a = C_{11}/C_{44}$ and $b = C_{12}/C_{44}$. Dashed lines indicate loci of points with constant values of the anisotropy factor $\Delta = a - b - 2$. Thick lines represent thermodynamic constraints on a and b.

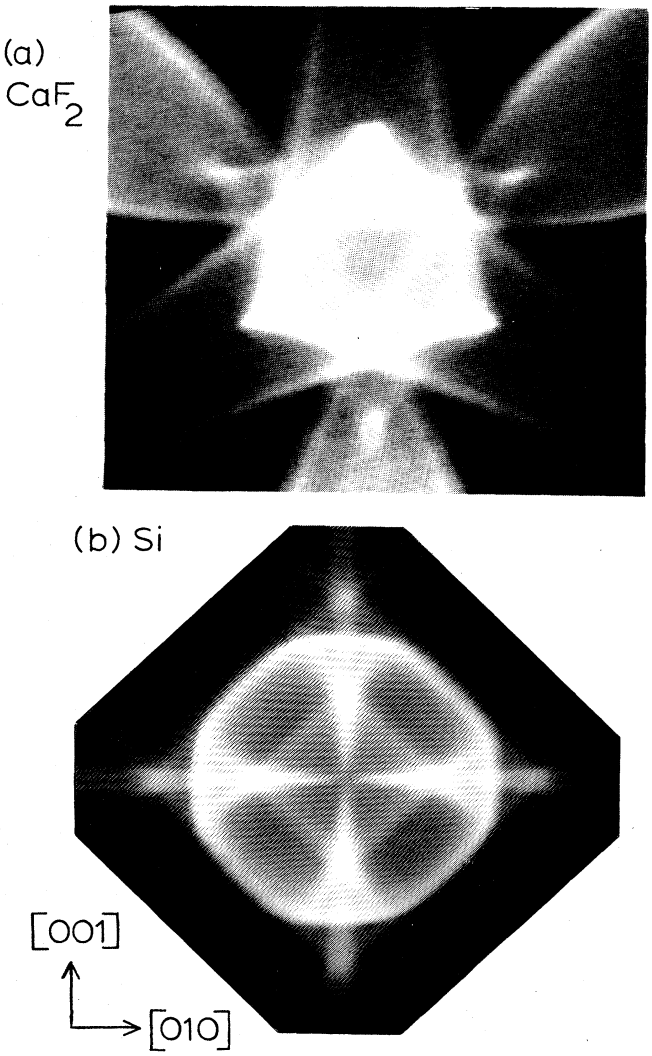

FIG. 2. (a) Experimental heat-pulse image for CaF_2, centered on the [111] direction. The image spans ±23° left to right. (b) Phonon image for Si, centered on the [100] direction and spanning ±12°. These phonon images were recorded using a broad time gate so that both transverse phonon modes were included.

In the past it has been shown that an effective way of understanding a particular crystal's focusing pattern is by constructing in wave-vector space the constant-frequency, or slowness, surface for each of the three acoustic modes in that material—one longitudinal and two transverse.[3,22–24] (Technically, there is only one slowness surface composed of three sheets.) Since all real crystals are elastically anisotropic, the surfaces are nonspherical. An immediate consequence is that a **k** vector defining a particular point on the slowness surface is not usually parallel

to the corresponding group-velocity vector, $\mathbf{V}=\nabla_k\omega(\mathbf{k})$, which is normal to the surface at that point. Thus, generally the energy flux associated with a given phonon is not collinear with its wave vector. This is how an isotropic angular distribution of $\mathbf{k}$ vectors, as produced by an ideal incoherent heat source, can produce an anisotropic concentration of energy flux—i.e., phonon focusing.

The topology and curvature of the slowness surface determine the kinds of focusing features that result in the thermal-flux intensity pattern. For a surface in three dimensions, the local curvature is conventionally described by a "Gaussian curvature" which is defined as the product of the two principal curvatures (inverse radii) of an element of surface at that point. In general, a section with large Gaussian curvature on the slowness surface indicates a "defocusing" of group-velocity vectors, or a reduction in phonon flux for the corresponding propagation directions. Likewise a flat section of the slowness surface indicates that the corresponding wave vectors have their energy "focused," or concentrated, along a narrow angular region in real space. The slowness surface for a given crystal contains sections of positive (convex or concave) and negative (saddle) curvature, separated by lines with zero Gaussian curvature. These lines of vanishing curvature ("parabolic lines") on the slowness surface correspond to the real-space caustics of mathematically infinite phonon flux. The boundaries of the bright features in the phonon images of Fig. 2 are such caustics. Clearly, a study of the slowness surface provides insight into the kind of intensity pattern formed.

For a surface in $\mathbf{k}$ space of constant frequency ω_0, the distance from the origin to a point on this surface is $k=\omega_0/v(\mathbf{k})$, where $v(\mathbf{k})$ is the phonon phase velocity. Similarly, the slowness surface is defined as $s(\mathbf{k})=k/\omega_0=1/v(\mathbf{k})$. The slowness surface is therefore constructed by calculating the inverse phase velocity for all angles in $\mathbf{k}$ space. The phase velocity v is obtained from the Christoffel equation,[25] derived from continuum elasticity theory:

$$(D_{il}-v^2\delta_{il})\epsilon_l=0\ , \tag{1}$$

where ϵ_l is a Cartesian component of the phonon polarization vector, and $D_{il}=C_{ijlm}n_jn_m/\rho$ is the Christoffel tensor for the wave normal $\mathbf{n}=\mathbf{k}/k$ and the elastic tensor C_{ijlm}. The phase velocity for a given $\mathbf{k}$ is obtained by solving the characteristic equation of Eq. (1), which is cubic in v^2. Each root corresponds to a solution for one of the three acoustic phonon modes, and so the three sheets of the slowness surface can be generated. The slowness surfaces are graphically constructed by computing the inverse velocity for lines of constant θ_k and ϕ_k (standard polar coordinates) and then plotting these lines in the desired perspective. A root-finding program is used to determine the parabolic lines (thick lines in the drawings) and to project them onto the slowness surface.

Thus, an important part of this paper is to characterize the shapes of the slowness surfaces for realistic values of elastic constants. Just what shapes can slowness surfaces take on? Clearly, when $\Delta=0$ the surface is spherical, indicating perfect isotropy. For slightly positive or negative Δ, the surface becomes nonspherical. As the anisotropy is hypothetically increased, small regions of saddle or concave curvature develop. A preview of this evolution may be found in Figs. 7, 10, and 17. The shaded regions represent saddle curvature. For the most part, the ⟨100⟩, ⟨110⟩, and ⟨111⟩ symmetry directions act as sources for these new saddle and concave regions. As anisotropy is increased, the advent of a new region of different curvature is signaled by a change in the sign of the Gaussian curvature near the symmetry direction. Correspondingly, new features will appear in the phonon flux pattern at these critical values of elastic constants.

Every and others[15,26–28] have examined the conditions on the elastic constants which are necessary for specified regions of the slowness surface to have vanishing curvature. For some symmetry planes, near specific symmetry directions, the two principal curvatures can be expressed in terms of the phase velocity, and thus in terms of the elastic constants. The combinations of elastic constants that yield zero or negative values for either the in-plane or transverse curvature at these specific directions can therefore be determined. When mapped into elastic-parameter space, these conditions on the elastic constants form a set of curves as shown in Fig. 3. For brevity we will refer to these curves as "critical curves," i.e., curves with critical values of elastic constants that signal the advent of a new feature in the surface topology. For each successive region away from the $\Delta=0$ line, the topology becomes more complex. The specific set of critical curves for each mode is discussed below.

(1) Longitudinal (L) mode. For cubic crystals, the longitudinal slowness surface is entirely convex,[29] so there are *no* caustics due to L-mode phonons in the phonon intensity patterns. There *is* an anisotropy of phonon flux, since the curvature of the slowness surface varies somewhat, producing maximum flux in regions of minimum (but still positive) curvature. The slowness surfaces for the L mode in CaF_2 and Cu are shown in Figs. 4(a) and 4(b), respectively. For positive-Δ materials (such as CaF_2), the surface curvature is a minimum in the ⟨100⟩ directions, so that in these directions the phonon flux is most intense. For negative-Δ crystals (such as Cu), the surface bulges out in the ⟨100⟩ directions and is flattest in the areas near and between adjacent ⟨111⟩ directions. Thus the phonon flux is reduced near the ⟨100⟩ directions, and enhanced between adjacent ⟨111⟩ directions. Since these anisotropic effects are relatively small and no flux singularities occur, the L mode will not be discussed further.

(2) Slow transverse (ST) mode. The critical curves which signal changes in the slowness-surface topology for the ST mode are shown in Fig. 3(a). In terms of the variables a and b, the equations for the critical curves as labeled are as follows:[15] For curve A,

$$2(a-1)(b+1)+(a-b-2)(a+2b+1)\times(2a+b-1)=0\ , \tag{2}$$

for curve B,

$$a(a-1)-(b-1)^2=0\ , \tag{3}$$

for curve C,

$$a^2+(a-1)(b+1)-2(b+1)^2-1=0\ , \tag{4}$$

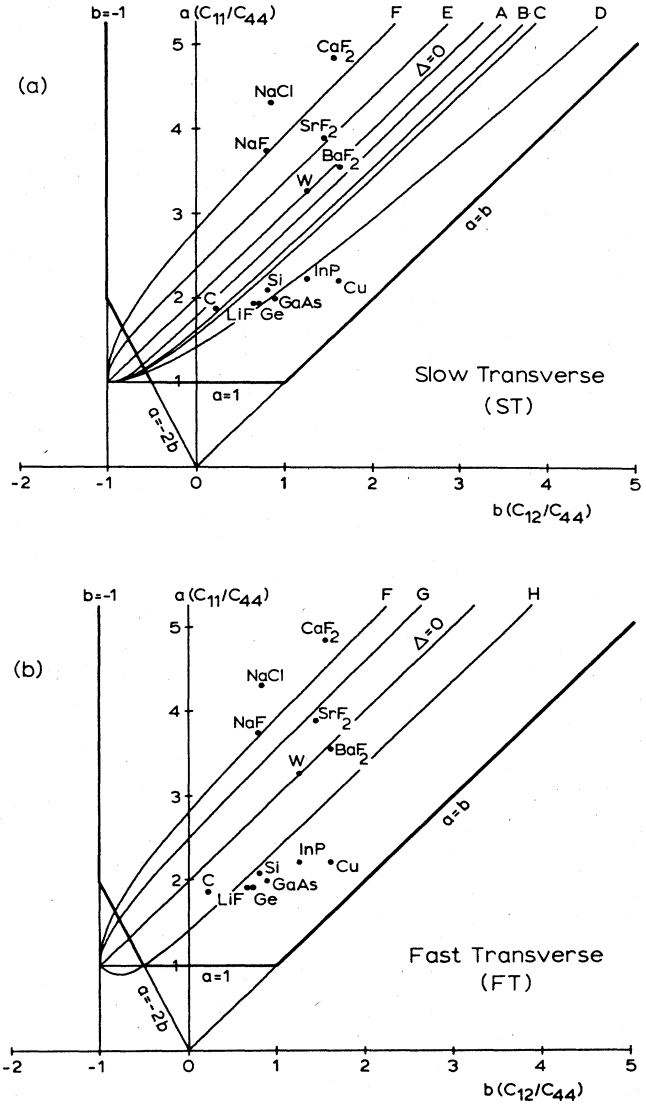

FIG. 3. Elastic-parameter space. (a) Lines A through F are the critical curves discussed in the text which signal qualitative changes in the ST-mode slowness surface. (b) Curves F through H represent critical changes in the FT-mode slowness surface.

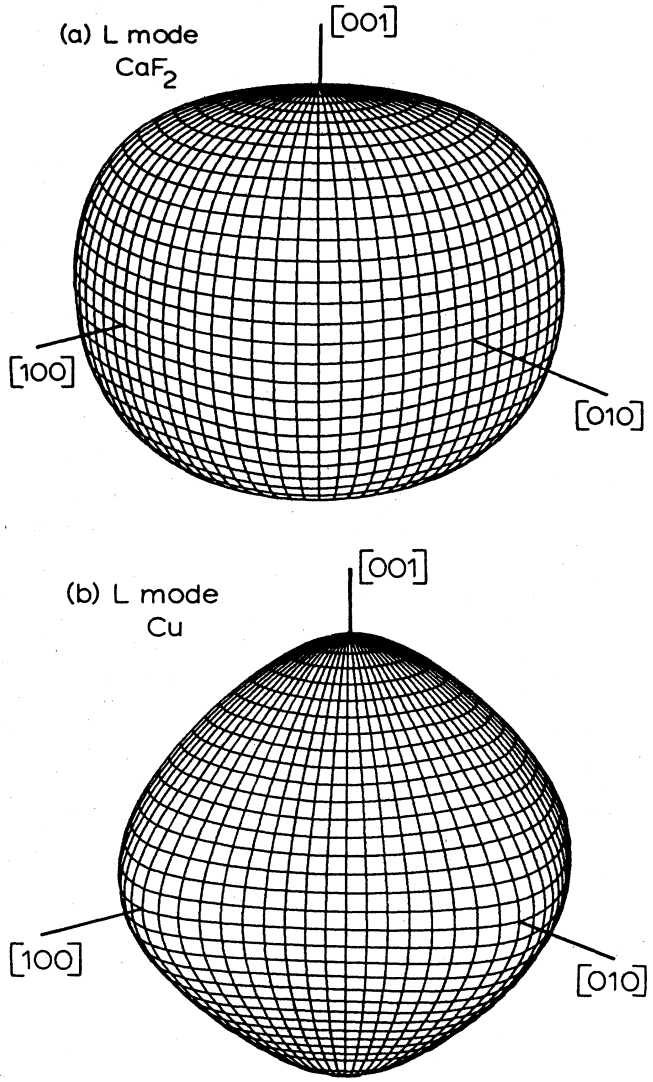

FIG. 4. (a) Slowness surface for L phonons in CaF_2. The curvature is a minimum around ⟨100⟩, and a maximum near ⟨111⟩. (b) Slowness surface for L phonons in Cu. Areas of minimum positive curvature reach between adjacent ⟨111⟩ directions.

for curve D,

$$(a-1)(a+b)+(a-b-2)(b+1)^2=0\ , \tag{5}$$

for curve E,

$$2a^2-3a+ab-3b^2-9b-4=0\ , \tag{6}$$

and for curve F,

$$6(a-b+1)^2(b+1)-3(a-b-2)^2(b+1)$$
$$-(a-b+1)(a-b-2)(8a+13b+5)=0\ . \tag{7}$$

(3) Fast transverse (FT) mode. For the FT mode, there are three critical curves. The curve labeled F in Fig. 3(b) is identical to curve F in Fig. 3(a) and is described by Eq. (7). The other two curves shown in Fig. 3(b) are determined by the following equations: For curve G,

$$(2a+b-1)(a-b-2)-2(b+1)=0\ , \tag{8}$$

for curve H,

$$a^2+ab-2(b+1)^2=0\ . \tag{9}$$

As one moves away from the $\Delta=0$ line, each critical curve signals the advent of a new development in the slowness-surface topology, and thus a new development in the associated phonon intensity pattern. The evolution of the slowness-surface curvature can be summarized as follows: the critical curves for the ST sheet in the negative-Δ regime all denote changes in curvature that occur in the immediate vicinity of the ⟨100⟩ directions. For negative Δ, the single FT critical curve (denoted H) marks the advent of saddle regions between adjacent ⟨100⟩ directions. On the other hand, the critical curves for the positive-Δ

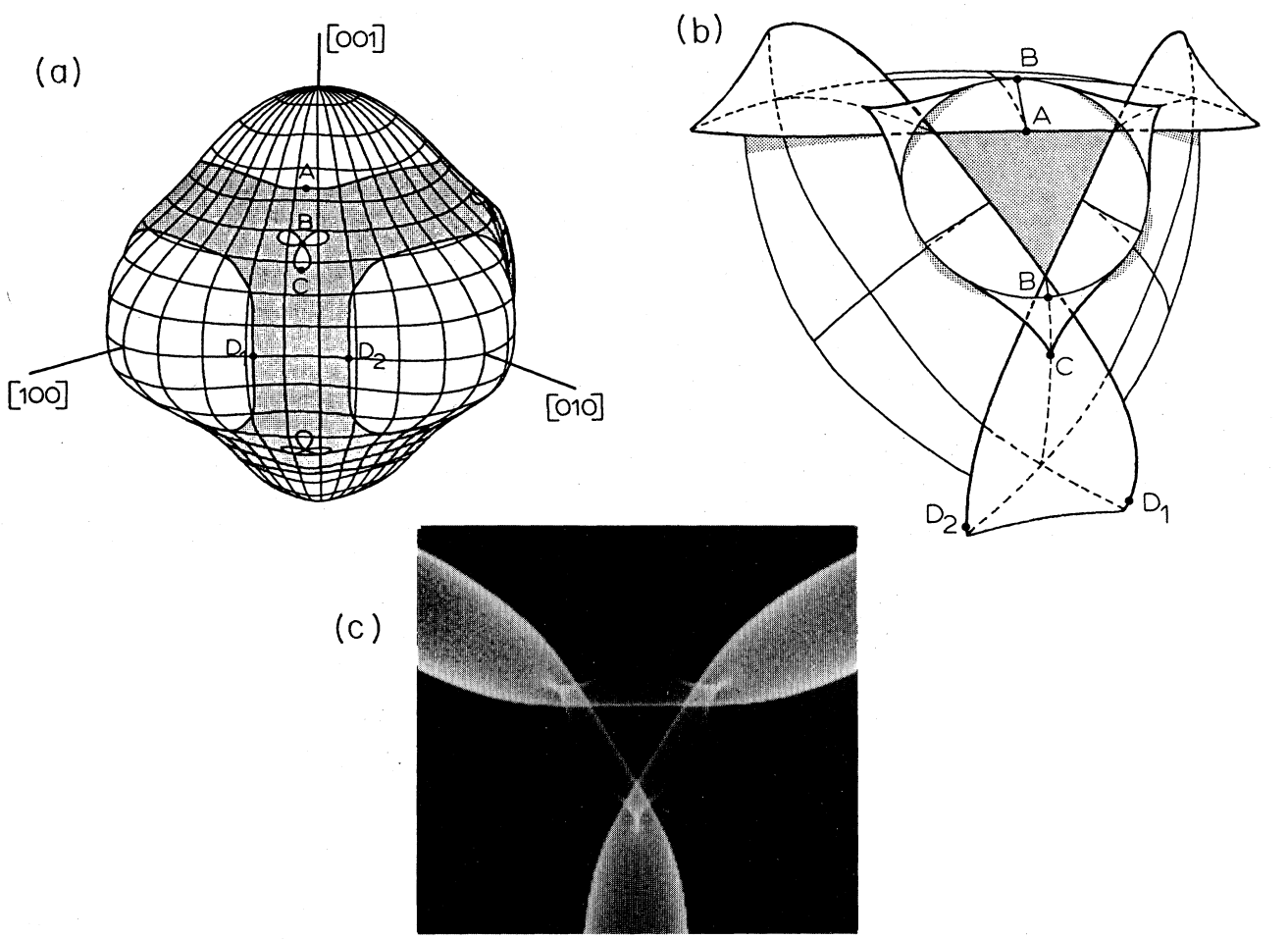

FIG. 5. (a) FT slowness surface for CaF_2. Phonons with **k** vectors at points *A* through *D* on this surface are focused into points *A* through *D* on the group-velocity surface in (b). Shading indicates areas of saddle (negative) curvature. All other portions of this surface are convex. Thick lines outlining saddle regions represent lines of zero Gaussian curvature and correspond to folds in the group-velocity surface. (b) Representation of the FT group-velocity surface near the [111] direction. No phonons are focused into the central shaded region. Thick lines represent folds which correspond to lines of mathematically infinite flux intensity (caustics). (c) Monte Carlo flux-intensity simulation for FT phonons in CaF_2. This image is centered on [111] and represents a scan of ±35° from left to right.

regime signal a change in the sign of the Gaussian curvature at one of three symmetry directions: curve *G* marks small new saddle regions at the ⟨110⟩ directions; curve *E*, at the ⟨100⟩ directions; while curve *F* is associated with the ⟨111⟩ directions.

In addition to an analysis of the slowness surface, it is useful to simulate the phonon-flux intensity pattern for arbitrary values of *a* and *b*. To produce the simulations, a computer program is used to map a uniform-probability, random distribution of phonon **k** vectors into (real-space) group-velocity vectors **V**. The **V** vectors are then projected onto a plane normal to the desired viewing direction, corresponding to the crystal surface across which a laser beam would be scanned. The intensity at one pixel—i.e., the number of **V** vectors mapped into that pixel—is stored in a 256×256 element array. An image array with an integrated intensity of approximately 10^6 phonons typically takes 20 min of computing time on a VAX 730 computer. The image array can be transferred to a video frame buffer which displays the result on a video monitor. Photographs of the monitor screen are presented here.

Another construction helpful in understanding these focusing patterns is the group-velocity surface, or wave surface. Physically, the wave surface represents the shape of a wave front caused by a point disturbance in the medium. This surface is formed by calculating the group velocity **V**, or surface normal, for points on the slowness surface. For a given real-space direction, the distance from the origin to the wave surface equals the magnitude of **V**. Thus group-velocity surfaces are closely related to energy-flux simulations, but have the added feature of being a three-dimensional representation of the wave front.

III. CRYSTALS WITH POSITIVE Δ

A. An example—Calcium fluoride

A good example of a cubic crystal in the positive-Δ regime is CaF_2. Its focusing pattern possesses all of the

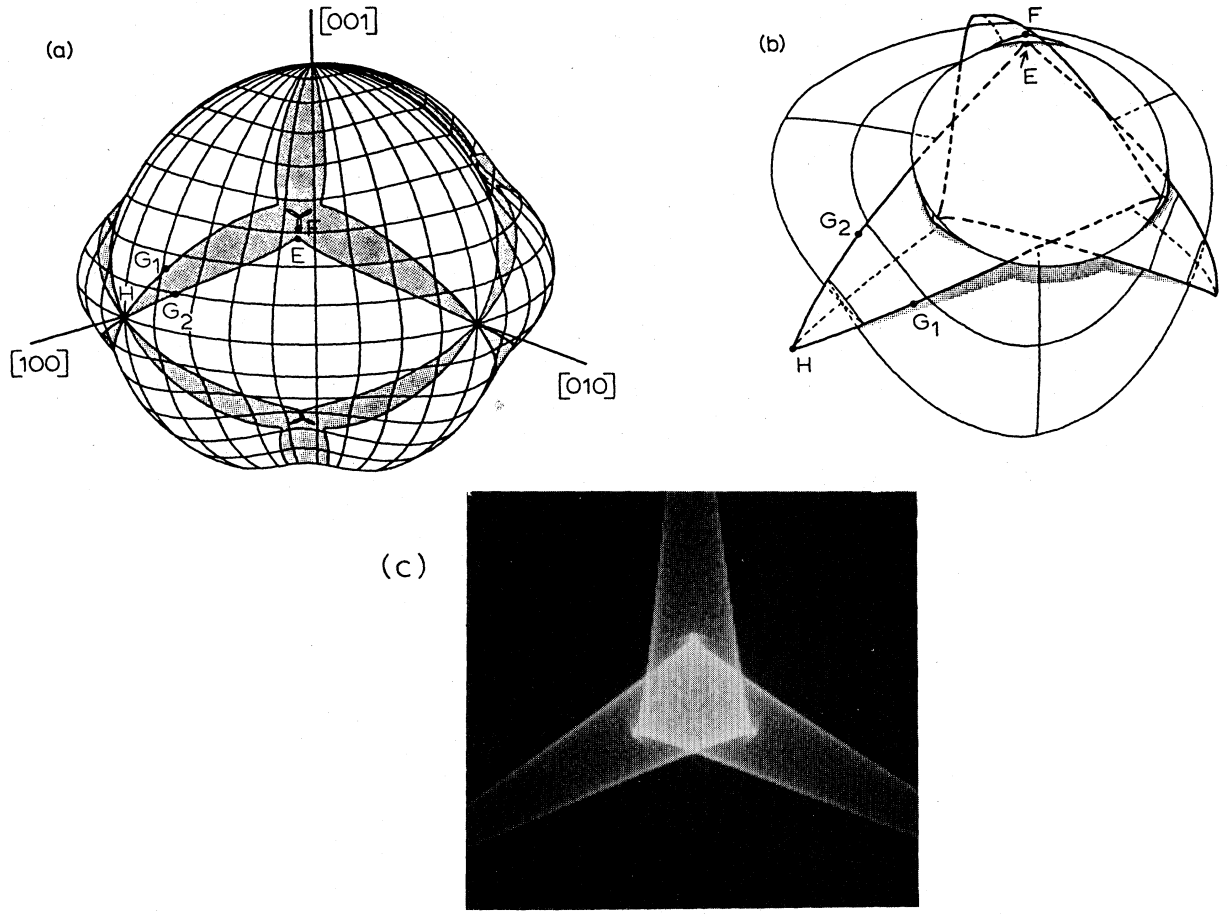

FIG. 6. (a) ST slowness surface for CaF_2. Points E through H on this surface correspond to points E through H on the velocity surface in (b). The three small areas forming the cloverleaf structure near $\langle 111 \rangle$ are concave. (b) Portion of the ST-mode group-velocity surface near the [111] direction. (c) Monte Carlo simulation for ST phonons. The image is centered on the [111] direction, and represents a scan of $\pm 35°$ left to right.

structures associated with this regime, for in elastic-parameter space CaF_2 lies beyond all critical curves. An experimental image of the focusing pattern for CaF_2 was shown in Fig. 2(a). The origin of this complicated pattern may be understood by examining the slowness and wave surfaces for CaF_2. The FT-mode slowness surface and a portion of the corresponding group-velocity surface are depicted in Figs. 5(a) and 5(b), respectively. Points A through D on the group-velocity surface correspond to similarly labeled points on the slowness surface. (These labels are not related to the critical curves in Fig. 3.)

On the slowness surface, starting from the [001] direction and moving toward point A, the surface is convex. The large curvature implies a defocusing of phonons, with a reduced phonon intensity. At point A, a change in the sign of the Gaussian curvature causes a fold caustic in the velocity surface. As $\mathbf{k}$ moves further toward the [111] direction (toward point B), phonons in the saddle region are channeled up away from the fold. Point B is a conic point where the ST and FT slowness surfaces meet, and the curvature is not defined at this point. As $\mathbf{k}$ is smoothly rotated through this point, the group-velocity vector suddenly flips to the opposite point on the conic circle, as shown in Fig. 5(b). For $\mathbf{k}$ just beyond point B, the slowness surface has convex curvature. At point C, the Gaussian curvature changes back to saddle, giving rise to the cusp in the wave surface.

The Monte Carlo simulation in Fig. 5(c) shows the heat-pulse intensities associated with the FT mode. The three-cusped structure, as also seen in the experimental image [Fig. 2(a)], is quite prominent. It is interesting to note that the roughly circular fold which joins the cusps does not exist entirely on the FT sheet. Instead, the fold extends between the FT and ST sheets, so that for each mode it appears as if there were three separate caustic lines which end on the conic circle. This phenomenon will be discussed in more detail below.

Figures 6(a) and 6(b) show the slowness and group-velocity surfaces associated with the ST mode. For $\mathbf{k}$ along the [110] crystalline direction, the slowness surface is convex and indicates a large defocusing of phonon flux. As $\mathbf{k}$ approaches the parabolic line at point E from below, the phonon group velocity points above the [111] crystalline direction, then nears a cusp caustic. As $\mathbf{k}$ is rotated

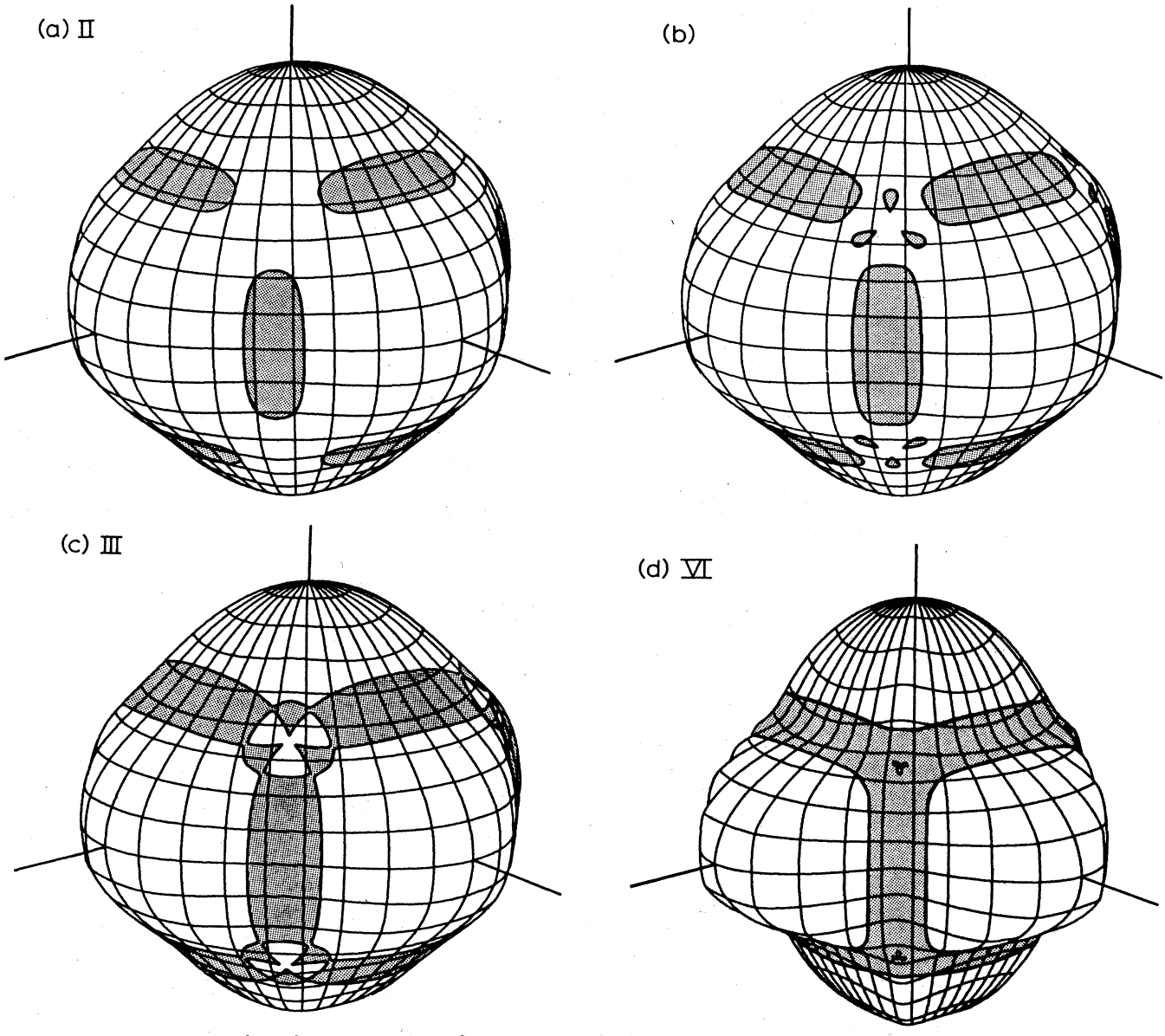

FIG. 7. FT slowness surfaces for several values of a and b in the positive-Δ regime, showing the topological changes with increasing anisotropy. The Roman numerals identify these elastic ratios in Fig. 9. The slowness surfaces were calculated using the following values: (a) $a=3.15$, $b=0.47$ (point II); (b) $a=3.18$, $b=0.43$; (c) $a=3.20$, $b=0.40$ (point III); and (d) $a=3.75$, $b=-0.50$ (point VI).

further toward point F, **V** now points up beyond the cusp. Phonons in the small island of *concave* curvature between point F and [111] possess velocity vectors that are directed back down towards the [111] direction. When **k** crosses the [111] direction, there is a discontinuity in the direction of **V**. Group-velocity vectors for phonons in the saddle region above the [111] direction point below the symmetry direction. The topology of the wave surface is directly reflected in the predicted heat-pulse intensities, which are shown by the Monte Carlo calculation of Fig. 6(c). The focusing pattern agrees well with that in the experimental image in Fig. 2(a).

One important aspect of the wave-surface topology in CaF_2 is that a fold in the total wave surface crosses the conic circle which joins the FT and ST sheets. This has interesting implications with regard to the heat-pulse intensity. The intensity on the conic circle is mathematically zero because this *line* corresponds to only one *point* on the slowness surface (namely, $\mathbf{k}\|\langle 111\rangle$). On the other hand, the folds give rise to mathematically infinite energy flux. Thus the collision of these two features would seem to give a mathematically undefined intensity. The experimental image shows only a weak intensity at these six points.

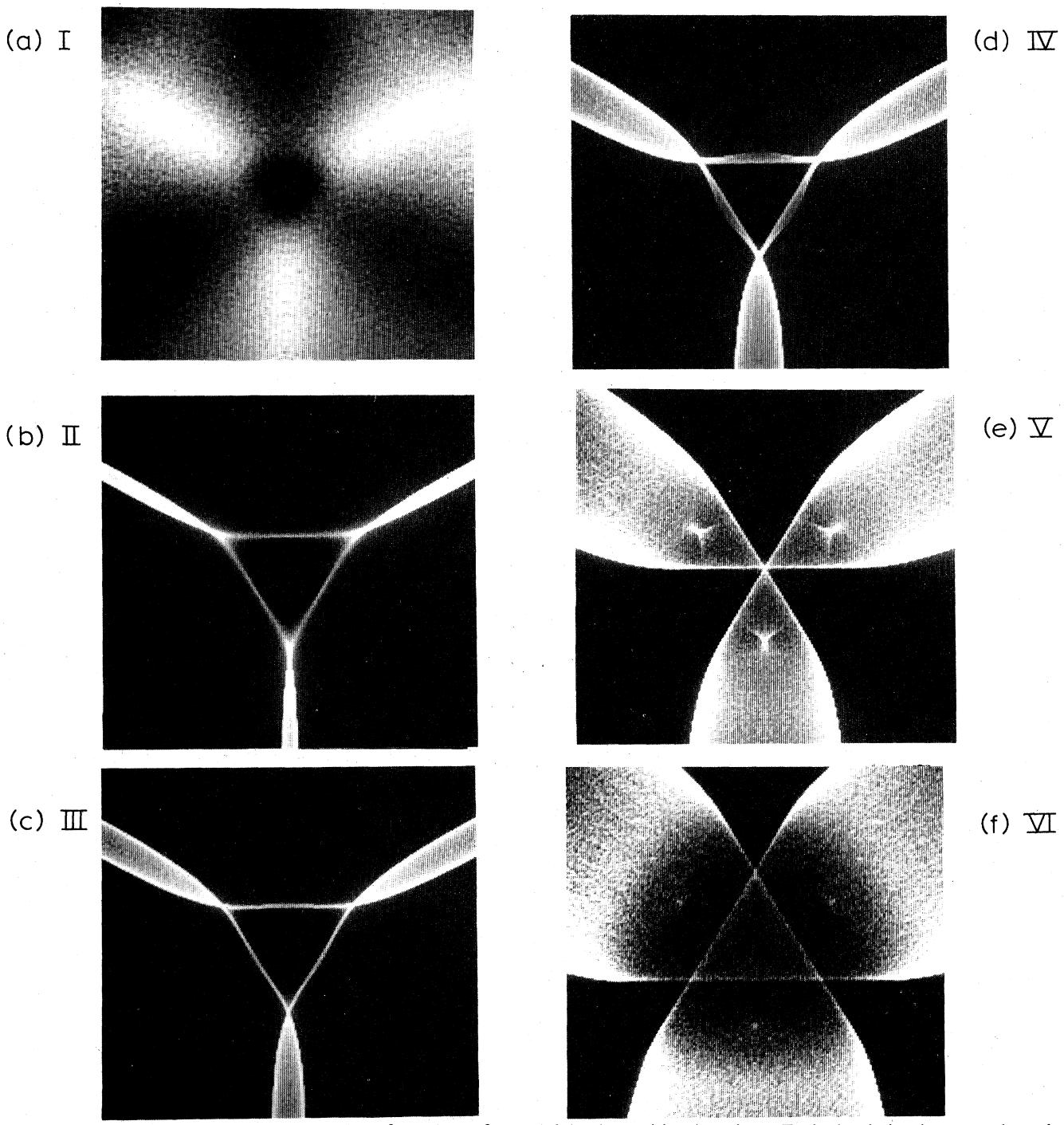

FIG. 8. FT-mode Monte Carlo simulations for values of a and b in the positive-Δ regime. Each simulation is centered on the [111] crystalline direction and spans $\pm 35°$ left to right, so that the [110] direction lies at the center of the lower edge of the images. The combinations of a and b used in the simulations are labeled as points in Fig. 9. The simulations were calculated with the following values: (a) $a=2.95$, $b=0.65$ (point I in Fig. 9); (b) $a=3.15$, $b=0.47$ (point II); (c) $a=3.20$, $b=0.40$ (point III); (d) $a=3.25$, $b=0.35$ (point IV); (e) $a=3.54$, $b=0.00$ (point V); and (f) $a=3.75$, $b=-0.50$ (point VI).

B. Fast transverse mode—General considerations

The series of calculations shown in Fig. 7 depicts the development of the FT slowness-surface topology for materials in the positive-Δ regime. The Monte Carlo flux-intensity simulations shown in Fig. 8 show the corresponding evolution in the focusing structures near the [111] direction. The values of a and b used to generate the Monte Carlo simulations are plotted in Fig. 9 as points I—VI. (The rest of the figure is explained below.) These calculations are for arbitrary values of a and b that

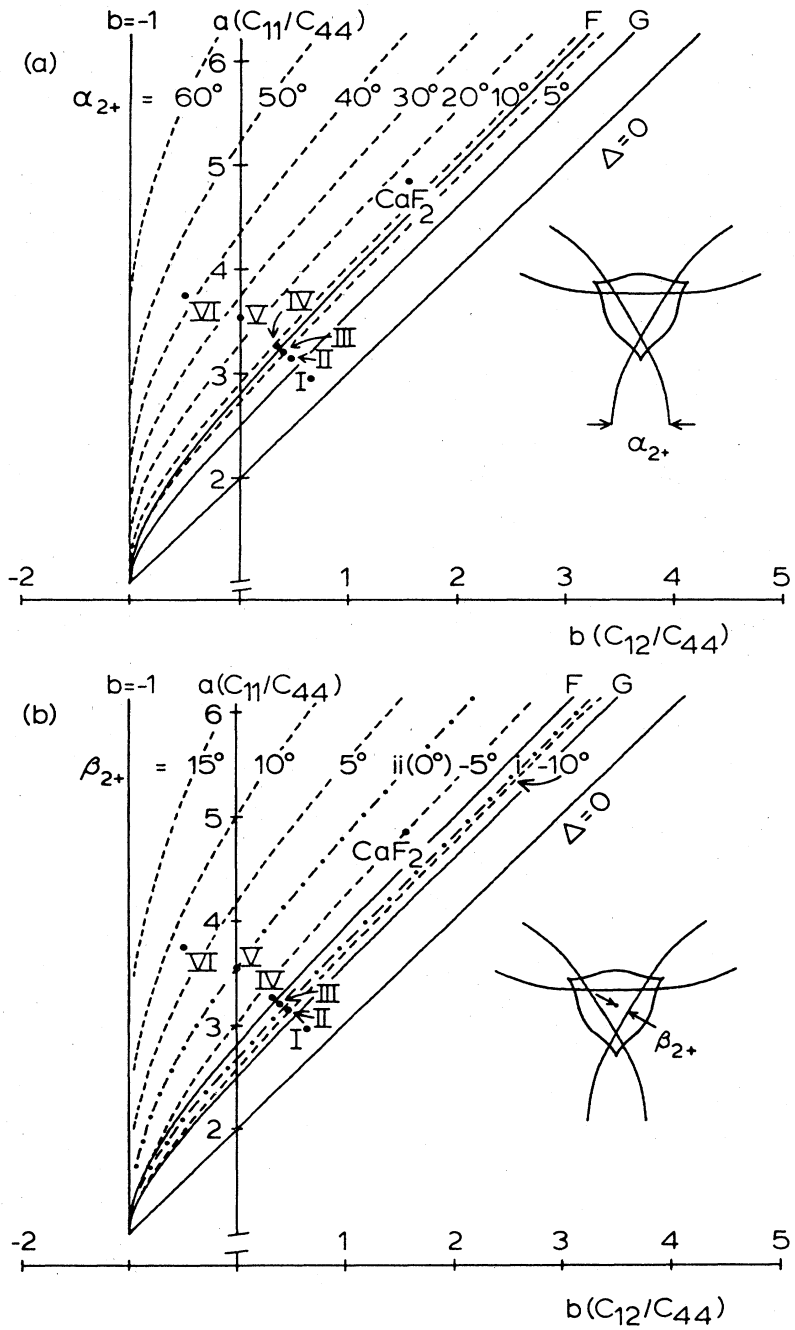

FIG. 9. Curves in elastic parameter space which show constant values of the two FT-mode, positive-Δ angular dimensions. (a) Curves of constant α_{2+}, defined as the real-space angle subtended by the two fold caustics as they intersect the (001) plane, as indicated in the inset. (b) Similar curves for β_{2+}, defined as the angle between ⟨111⟩ and the midpoint of a leg in the ⟨111⟩-centered triangle. The simulations in Figs. 8(d), 8(e), and 8(f), respectively, show the cases for which β_{2+} is negative (no phonons propagate near ⟨111⟩), zero, or positive (phonons propagate inside the caustics). The dashed-dotted line labeled i indicates the ratios beyond which the intense triangular structure becomes singular.

do not represent particular materials, but point out significant steps in the development of the focusing pattern.

For materials near the $\Delta=0$ line, the slowness surface is entirely convex. Least convex are the regions between adjacent ⟨111⟩ directions, so that the flux is most intense there. The Monte Carlo simulation for point I in Fig. 8(a) displays this behavior. Increasing the anisotropy and crossing curve G in Fig. 9 causes saddle regions to develop in the slowness surface around the ⟨110⟩ directions [point II, Fig. 7(a)], and produces a singular structure shown in Fig. 8(b). The caustics are linked by a narrow triangular region of intense flux which does not con-

tain caustics. As the anisotropy is increased to approach critical curve F, the lobes of saddle region widen and lengthen, and smaller droplet-shaped areas of saddle curvature arise between the lobes, as seen in Fig. 7(b). The parabolic lines bounding the droplets produce three small fold structures which contribute to the ⟨111⟩-centered triangle. For increased anisotropy, the droplet-shaped areas on the slowness surface merge with the lobes, leaving a convex "island" at the [111] direction. In this case, the parabolic lines bounding the island give rise to a continuous caustic with three cusps that encircles the symmetry direction. The slowness surface and flux-intensity simulation for this case (point III) are shown in Figs. 7(c) and 8(c), respectively. The cusps are not visible in Fig. 8(c) because they fall very close to the vertex of the triangle formed by other caustics.

At curve F, the parabolic lines bounding the island on the FT surface just touch the [111] direction. Thus, beyond curve F, each large island splits into three separate sections that meet at the [111] conic point. [We will see that curve F also marks the emergence of parabolic lines from the conic point on the ST sheet. One can imagine the FT parabolic lines continuing through the conic point to form the ST "cloverleaf" in Fig. 6(a).] The result in real space is that the continuous caustic containing the three cusps splits into three sections, each containing a cusp. This phenomenon occurs in the simulation in Fig. 8(d) (point IV), as well as in the simulation for CaF_2 [Fig. 5(b)]. In fact, the missing parts of this parabolic line have moved to the ST sheet via the conic point. As anisotropy is increased beyond curve F, the convex islands shrink in size [Fig. 7(d), point VI]. However, the curvature of these islands increases with increasing anisotropy, so that the position of the cusps relative to the symmetry direction remains fairly constant, as seen in Figs. 8(e) and 8(f).

Notice that in Fig. 8(d) *no* FT phonons propagate inside the bright ⟨111⟩-centered triangle. As Δ is increased, this triangle gradually shrinks until it disappears [Fig. 8(e)] and FT phonons can propagate in the [111] direction. As Δ is increased further, a triangular region containing multiple wave sheets appears about the [111] direction, as Fig. 8(f) shows.

Because the focusing structures vary smoothly with increasing Δ, it is possible to conceive of using one or two angular dimensions to quantitatively define the size of each focusing structure. For example, the angular separation between two related caustics can be determined for each point in the elastic-parameter space. We apply this concept first to the positive-Δ regime. For all materials located beyond curve G, there are always pairs of curved fold caustics that run along the ⟨110⟩ directions. The two caustics have a maximum separation when they intersect a {001} plane. Let the angle α_{2+} be defined as the angular width of the folded region bounded by two caustics at $\theta_V = 90°$, e.g., points D_1 and D_2 in Fig. 5(b). The angle α_{2+} is indicated in the inset in Fig. 9(a). [The 2 refers to the mode (1=ST, 2=FT); + refers to the sign of Δ.] The dashed curves plotted in Fig. 9(a) are calculated for constant values of α_{2+}. To obtain these curves, a fixed value of b was chosen and then a was adjusted to yield a selected value of α_{2+}. This angle was determined with an accuracy of $\pm 0.05°$. This procedure was repeated for different b at intervals of $\Delta b = 0.05$–0.1 until the desired (a,b) parameter space was covered.

A second dimension that helps to define the positive-Δ FT focusing structures is a measure of the size of the triangle of caustics surrounding the [111] direction, such as the angle β_{2+} indicated in Fig. 9(b). The elastic ratios which show the first appearance of singularities in the triangle (i.e., when the droplet-shaped saddle regions appear) are plotted in Fig. 9(b) as the dashed-dotted line marked i. The values of a and b for which the triangle has zero dimension [$\beta_{2+} = 0°$, as in Fig. 8(e)] are plotted as the dashed-dotted line marked ii in Fig. 9(b). The angle β_{2+} is that between the [111] direction and the propagation direction of a phonon at the midpoint of one leg of the surrounding triangle [such as point A in Fig. 5(b)]. We will denote all values of β_{2+} between curves G and ii as negative, indicating an "open" triangle (no phonons), as in the case in Fig. 8(d). Beyond curve ii, β_{2+} will have positive values, such as in Fig. 8(f). The dashed lines in Fig. 9(b) show the numerically calculated loci of elastic ratios for which $\beta_{2+} = -10°$, $-5°$, $5°$, $10°$, and $15°$. Given (a,b) for an arbitrary crystal, the simple determination of angles α_{2+} and β_{2+} from Figs. 9(a) and 9(b) makes it possible to quantitatively predict the directions of major flux singularities.

C. Slow transverse mode—General considerations

The evolution of the ST-mode focusing pattern for increasing Δ can be understood by examining both the series of slowness surfaces shown in Fig. 10 and the Monte Carlo simulations shown in Fig. 11. The images in Fig. 11 show the area within $\pm 35°$ of the [111] direction. The values of elastic ratios used to generate the Monte Carlo simulations in Figs. 11(a) through 11(c) are plotted in Fig. 12 as points I′ through III′, respectively.

The slowness surface in Fig. 10(a) and the flux-intensity simulation in Fig. 11(a) have been calculated for a hypothetical crystal with almost isotropic velocity (point I′). Although point I′ is located close to $\Delta = 0$, a small ⟨111⟩ three-cusped caustic structure such as that found in CaF_2 occurs. In fact, there is singular focusing of ST phonons for *all* positive-Δ materials. With increasing anisotropy, the saddle region surrounding each ⟨111⟩ direction grows, reaching towards the adjacent ⟨100⟩ directions. After curve E is crossed, the triangular saddle regions touch each other at the ⟨100⟩ directions, as indicated by the slowness surface in Fig. 10(b) for point II′. For increasing Δ, the saddle regions widen but always taper to a point at the ⟨100⟩ directions. The result in real space, as indicated by the intensity simulation of Fig. 11(b), is that the ⟨111⟩ cusp structures grow but the caustics meet in a point at the ⟨100⟩ directions.

When Δ is increased sufficiently to cross critical curve F, three small concave islands appear on the slowness surface near the ⟨111⟩. As noted in the discussion of CaF_2, the caustics formed by the parabolic lines bounding these islands are three small fold caustics located near the cusps [see Fig. 6(c)]. These fold caustics are the missing segments in the previously-mentioned FT-mode structure.

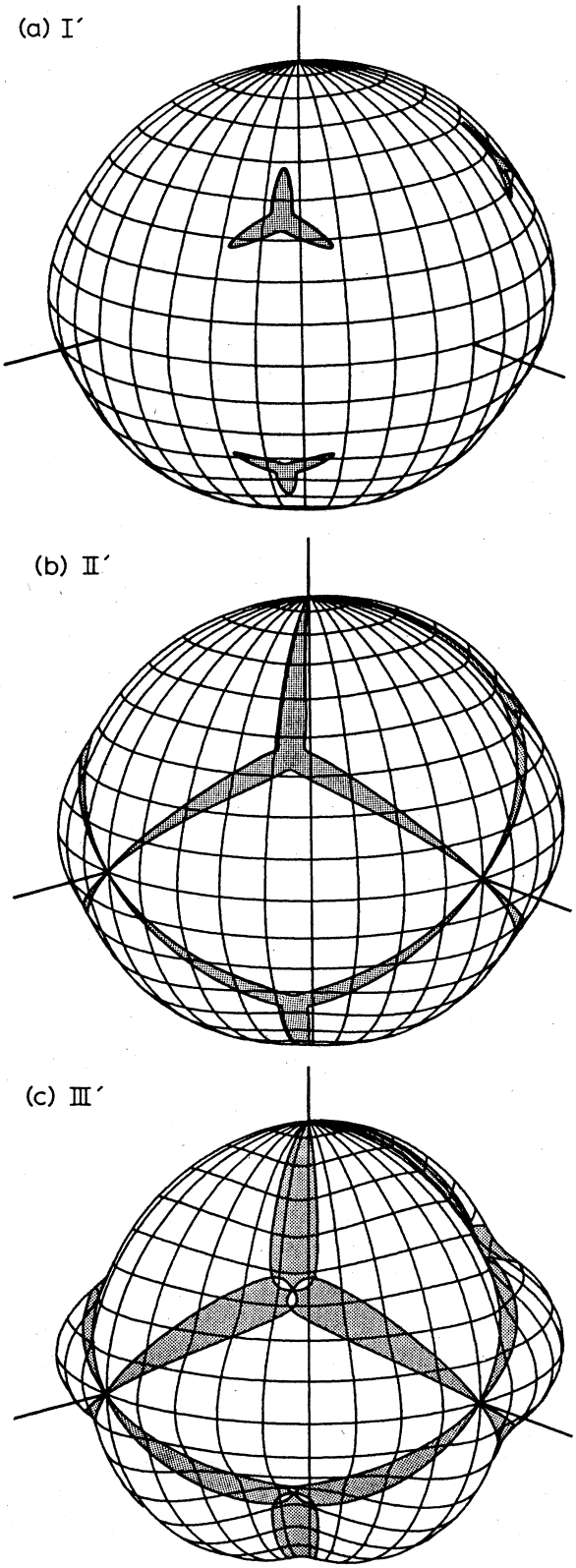

FIG. 10. ST slowness surfaces for several values of a and b in the positive-Δ regime. The values of a and b used are plotted as points in Fig. 12. The sets of elastic ratios used are as follows: (a) $a=2.95$, $b=0.65$ (point I′ in Fig. 12); (b) $a=3.00$, $b=0.60$ (point II′); and (c) $a=3.64$, $b=-0.19$ (point III′).

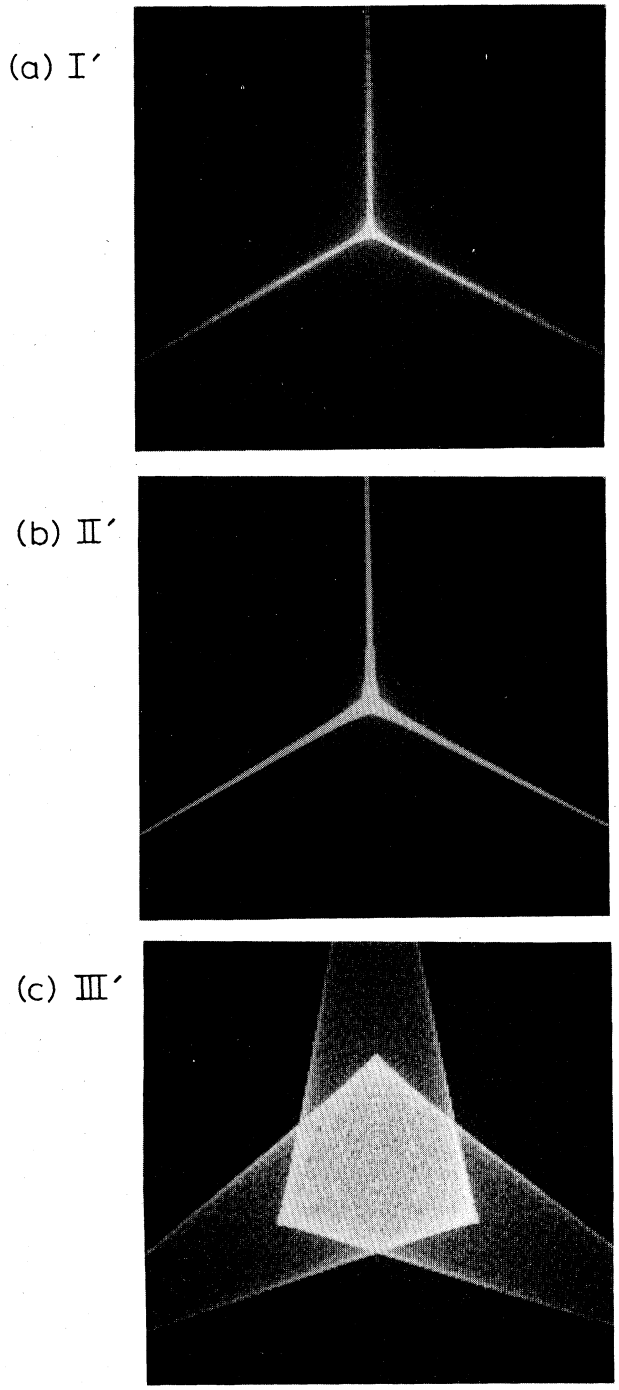

FIG. 11. ST-mode Monte Carlo simulations corresponding to the slowness surfaces in Fig. 10. The simulations are centered on the [111] direction and span ±35° left to right.

Comparison of the ST slowness surface for CaF_2 in Fig. 6(a) and that in Fig. 10(c) (point III′ in Fig. 12) shows that with increasing anisotropy beyond curve F, the concave islands expand in size until they almost touch the convex portions of the surface. The real-space result is not very dramatic, as the Monte Carlo of point III′ in Fig. 11(c) re-

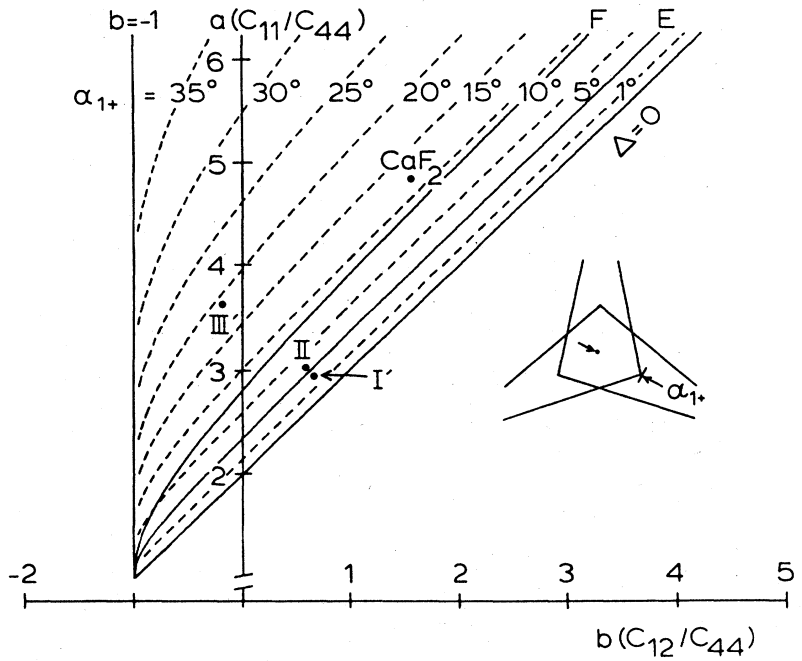

FIG. 12. Lines for which α_{1+} is a constant value. The ST-mode, positive-Δ characteristic dimension is defined as the angle between $\langle 111 \rangle$ and one of the cusp caustics, as indicated in the inset.

veals. The three-cusp structure has increased proportionately in size, but the three small fold caustics are hardly visible.

The major change in the ST focusing pattern can be characterized, as shown in Fig. 12, by defining the angle α_{1+} between the [111] direction and the propagation direction of phonons focused into a cusp. The plot in Fig. 12 shows curves of constant α_{1+} for values ranging from 1° to 35°.

In summary, the focusing structures which occur for the positive-Δ class of materials consist mainly of fold and cusp caustics centered around the $\langle 111 \rangle$ crystalline directions. The evolution of the principal FT and ST caustics can be sufficiently described with three angular dimensions. Figures 9 and 12 can be used to determine these dimensions for an arbitrary set of elastic constants.

IV. CRYSTALS WITH NEGATIVE Δ

A. An example—Silicon

The plot in Fig. 1 indicates that a number of cubic crystals previously examined by heat-pulse experiments—including Ge, GaAs, LiF, and Si—lie close together in elastic parameter space. Thus, the flux-intensity pattern of Si can be considered typical of these negative-Δ crystals. A magnified view of the experimental intensity pattern of Si was shown in Fig. 2(b). The $\langle 100 \rangle$ crystalline direction is at the center of the image, which spans about 24° left to right.

The slowness and wave surfaces for the two transverse modes of Si are shown in Figs. 13 and 14. The FT-mode intensity-pattern simulation in Fig. 13(c) reveals high-intensity "ridges"[3] which are bounded by a pair of fold

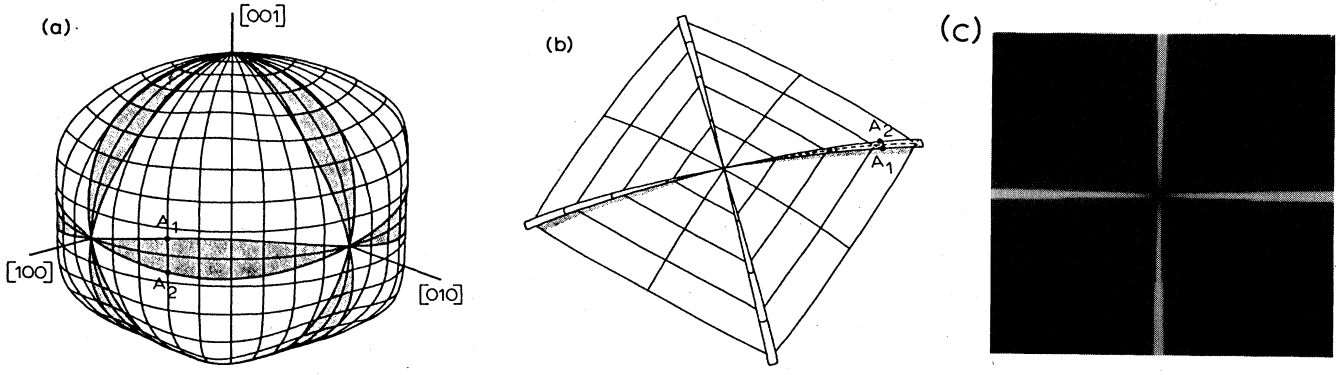

FIG. 13. (a) FT slowness surface for Si. Points A_1 and A_2 map into points A_1 and A_2 on the group-velocity surface in (b). (b) Section of the FT-mode group-velocity surface near the [100] direction. (c) FT-mode flux-intensity simulation for Si, centered on the [100] direction and covering a scan of ±45°.

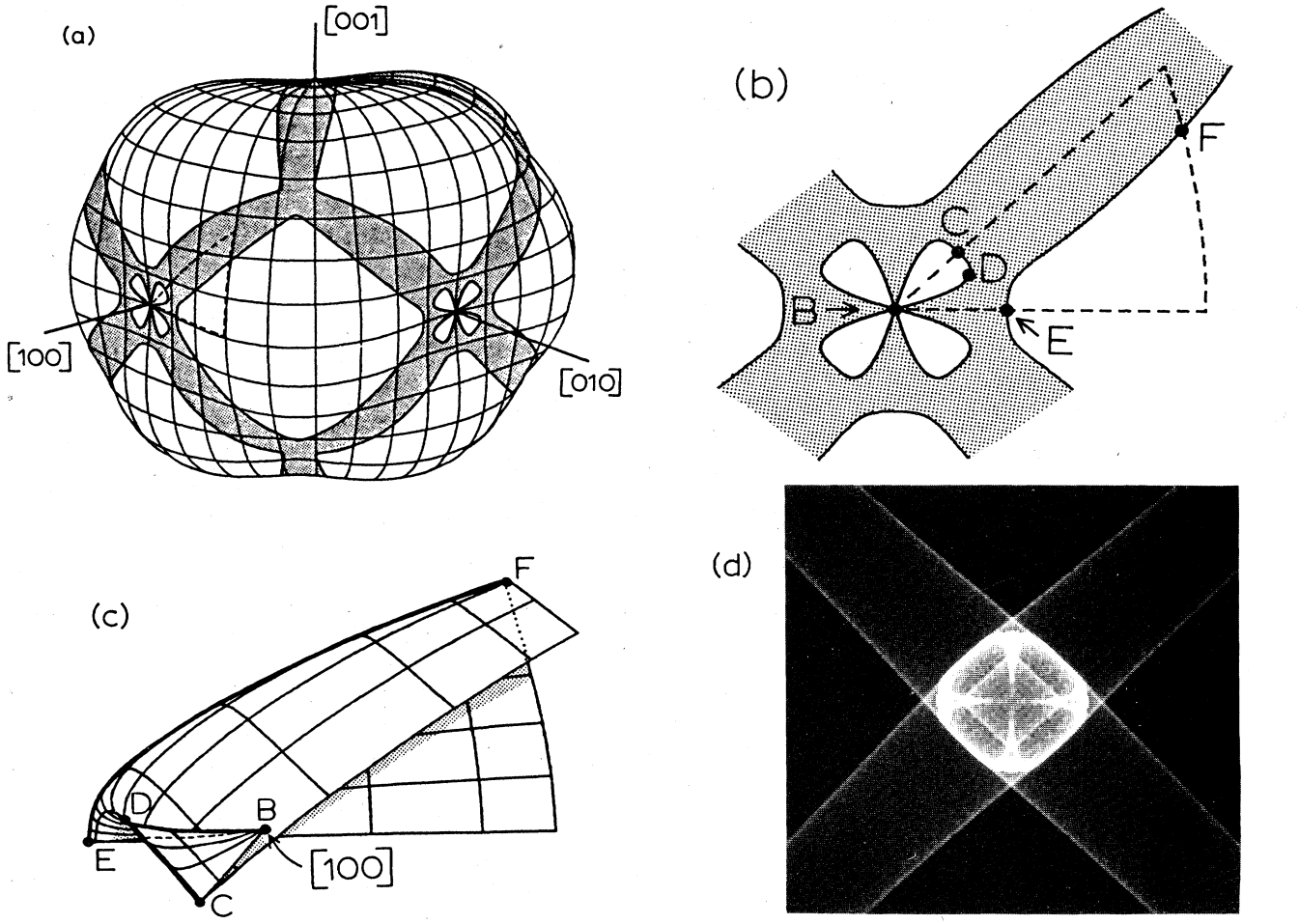

FIG. 14. (a) ST slowness surface for Si. The small cloverleaf sections of the surface surrounding each ⟨100⟩ direction are concave in curvature. (b) Symmetry-reduced portion of the ST slowness surface near [100]. The part of the surface enclosed by dashed lines maps into the portion of the group-velocity surface shown in (c). (c) Symmetry-reduced segment of the ST group-velocity surface for Si near the [100] crystalline direction. The remainder of the surface can be obtained by reflecting in (100) and (110) planes. (d) ST-mode flux-intensity simulation for Si, centered on the [100] direction and spanning ±20° left to right.

caustics in the wave surface [Fig. 13(b)]. The slowness surface [Fig. 13(a)] contains furrows of saddle curvature that extend between ⟨100⟩ directions.

The ST-mode intensity pattern is much more complicated, as shown in the Monte Carlo calculation in Fig. 14(d). The slowness surface for this mode in Si is depicted in Fig. 14(a). Present on this surface are fairly wide saddle regions that stretch between neighboring ⟨111⟩ and ⟨100⟩ directions. In the vicinity of the ⟨111⟩ directions, the ST slowness surface for negative-Δ crystals resembles that of positive-Δ crystals and causes similar three-cusp caustic structures in those areas [see Fig. 6(c)]. In addition, small concave "cloverleaves" occur directly around each ⟨100⟩ direction, which give rise to more folds and cusps.

Figure 14(b) is an enlargement of the slowness surface near the [100] direction. This portion of the slowness surface bounded by dashed lines maps into the section of the group-velocity surface shown in Fig. 14(c). This section is a symmetry-reduced segment of the complete wave surface near [100]. Points *B* through *F* in Figs. 14(b) and 14(c) show the point-to-point mapping of specific **k** vectors into real space. (The [100] axis passes through point *B*, while point *E* reaches 7° towards the [110] direction.) All of these features can be identified in Fig. 14(d). The fold lines *EF*, *DB*, and *DC* correspond to mathematical singularities in the flux and mark the intense flux regions. Notice that the line segment *EB* [partially represented by the dashed line in Fig. 14(c)] marks an edge of the wave surface which meets up with another symmetry-reduced section.

B. Fast transverse mode—General considerations

For elastic ratios between the $\Delta=0$ line and the curve labeled *H* in Fig. 3(b), the FT slowness surface is totally convex; there is no singular focusing of phonons. However, due to a local reduction in curvature, an enhanced flux appears between adjacent ⟨100⟩ directions. As $|\Delta|$ is increased beyond curve *H*, furrows of saddle curvature ap-

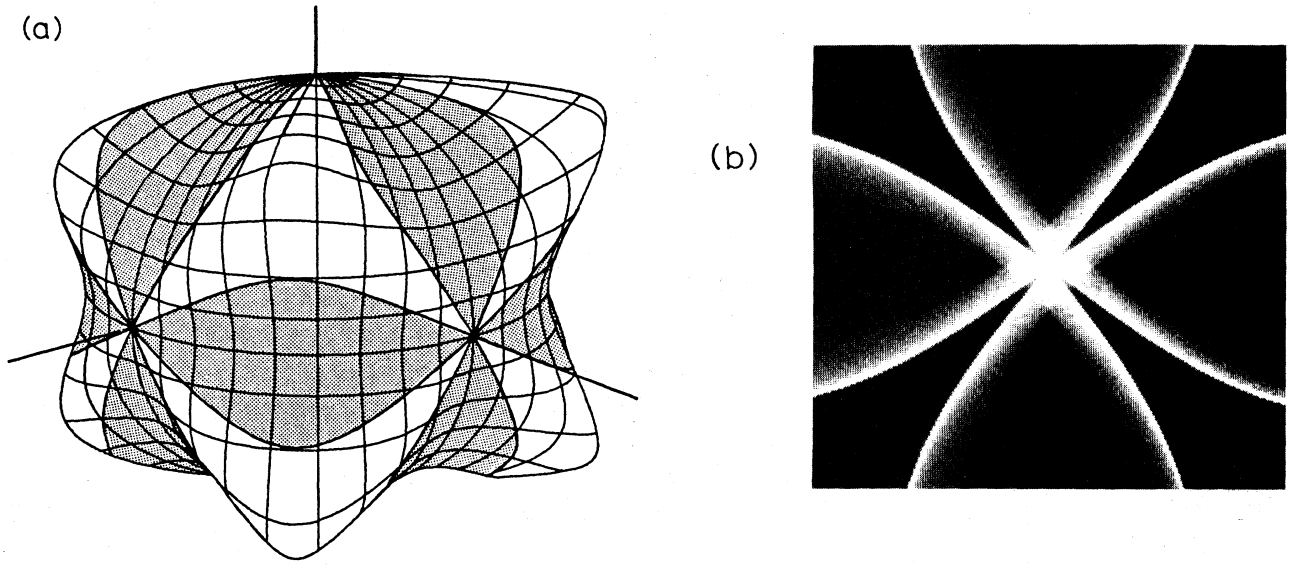

FIG. 15. (a) FT slowness surface for the point $a=1.60$, $b=1.40$ (negative-Δ regime). (b) Corresponding Monte Carlo simulation for FT phonons, centered on the [100] direction and spanning $\pm 45°$ left to right.

pear which run between adjacent $\langle 100 \rangle$ directions, as indicated in Fig. 13(a) for Si. These saddle regions produce the high-intensity FT "ridges." With increasing anisotropy, the saddle regions widen and become more deeply curved, as shown in Fig. 15(a). This causes a separation of the two caustics bounding the ridge in the intensity pattern, as shown in Fig. 15(b).

We define the angular dimension α_{2-}, as indicated in the inset in Fig. 16, as the angular separation between the two caustic lines at $\phi_V=45°$. The graph in Fig. 16 shows curves of constant α_{2-}. The focusing pattern for the FT mode is virtually identical for any two points on the same dotted line.

C. Slow transverse mode—General considerations

The fact that there are four critical curves for the ST mode in the negative-Δ regime [curves A through D in Fig. 3(a)] indicates that radical changes occur in the slowness-surface topology over this region. The evolution of this topology is represented by the series of slowness surfaces shown in Fig. 17. The Monte Carlo simulations

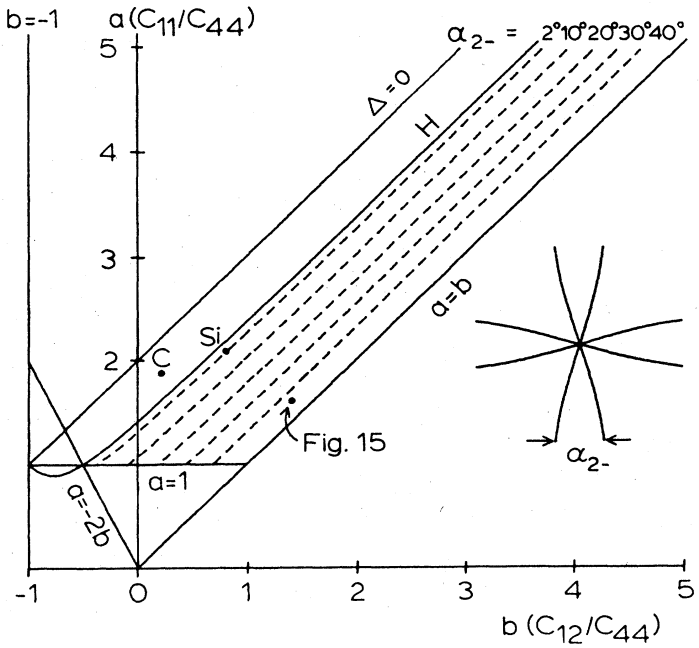

FIG. 16. Lines of constant α_{2-} in the negative-Δ regime. This angular dimension gives the maximum width of the FT ridge, as indicated in the inset.

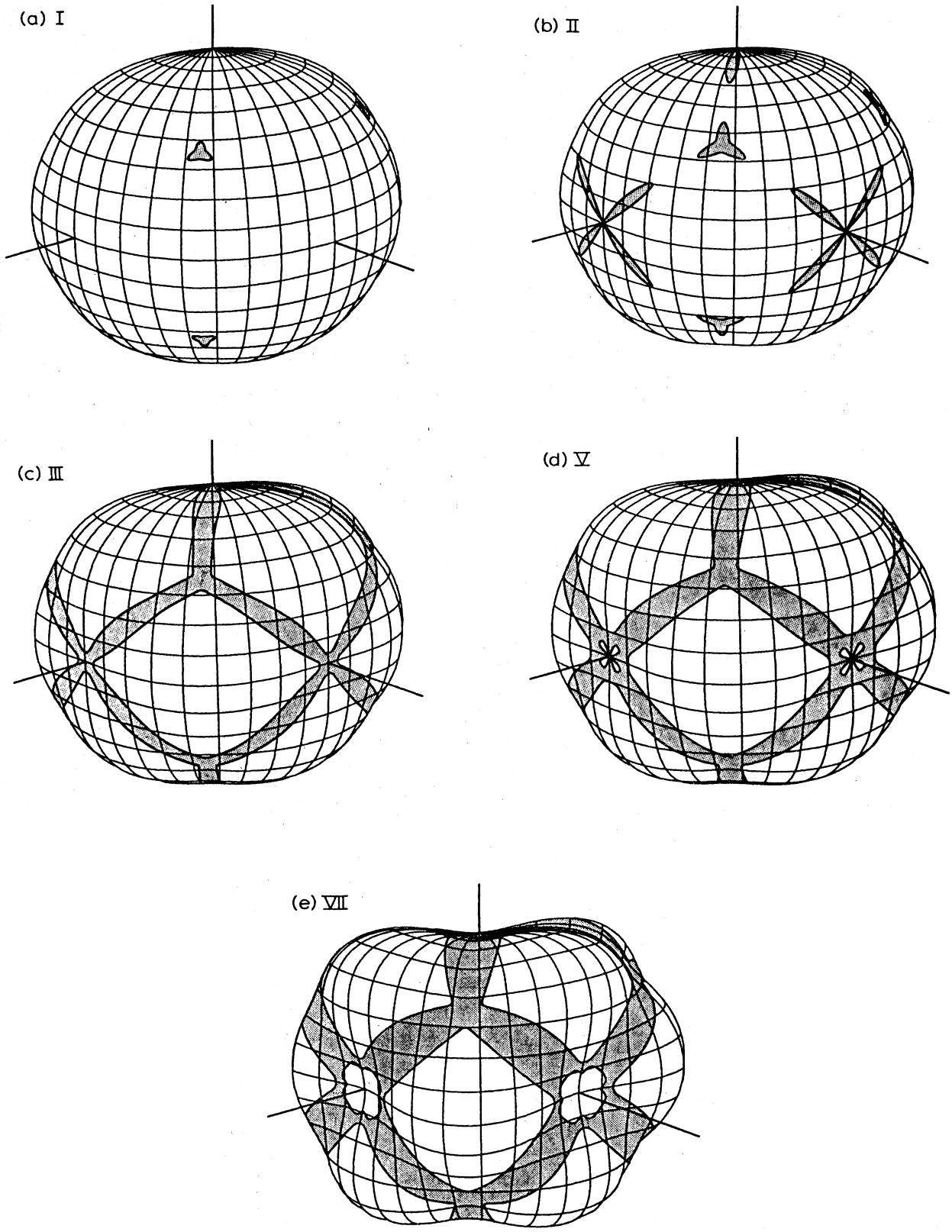

FIG. 17. ST slowness surfaces for the negative-Δ regime. The sets of ratios used in the calculations are indicated in Fig. 21. The following values of a and b were used to calculate the surfaces: (a) $a=2.40$, $b=0.60$ (point I); (b) $a=2.35$, $b=0.65$ (point II); (c) $a=2.275$, $b=0.725$ (point III); (d) $a=2.20$, $b=0.80$ (point V); and (e) $a=2.00$, $b=1.00$ (point VII).

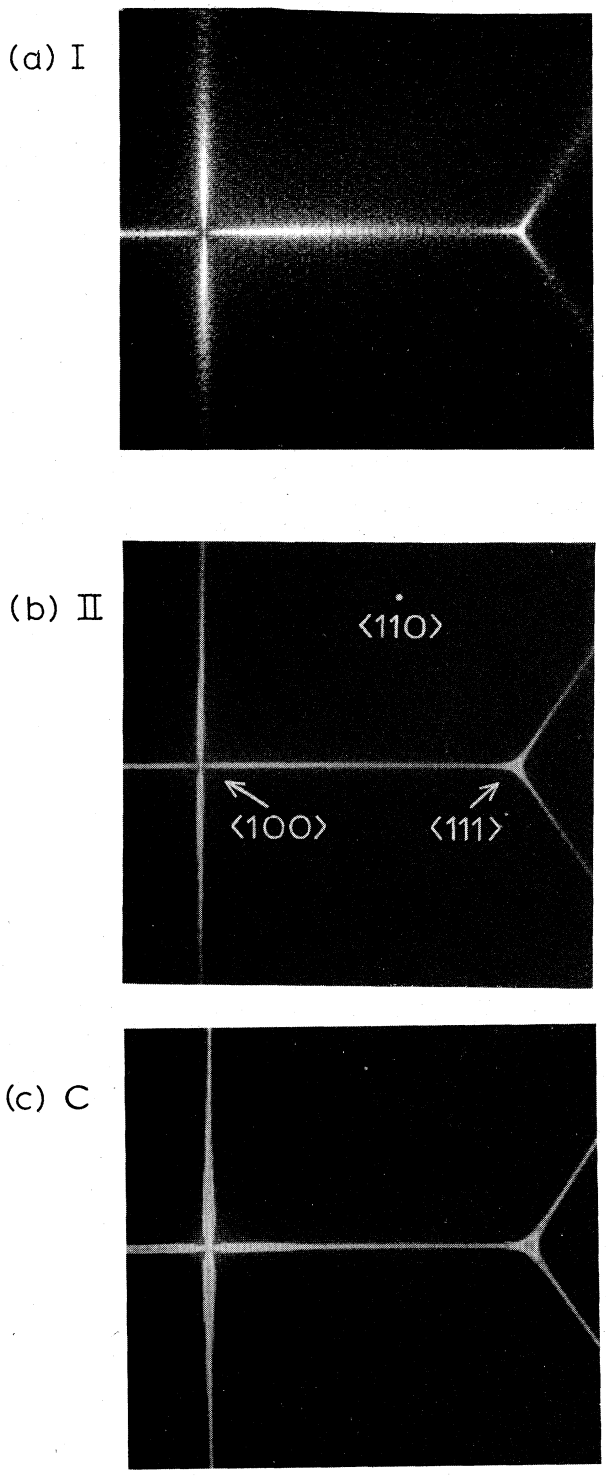

FIG. 18. ST-mode flux-intensity simulations for several negative-Δ elastic ratios. The elastic ratios used for the simulations have anisotropies between $\Delta=0$ and critical curve C, as shown in Fig. 21. The following elastic ratios were used: (a) $a=2.40$, $b=0.60$ (point I); (b) $a=2.35$, $b=0.65$ (point II); and (c) $a=1.87$, $b=0.22$ (diamond, C). The simulations are centered on the $[2\sqrt{2},1,1]$ crystalline direction and represent a scan of ±38° left to right.

in Figs. 18, 19, and 20 depict the corresponding development of the ST focusing pattern. The simulations in Fig. 18 were calculated assuming a $(2\sqrt{2},1,1)$ scanning surface, which includes both the [111] and [100] focusing structures. The simulations in Fig. 19 contain only the region within ±20° of the [100] direction, to examine more closely the complex structures there. The simulations in Fig. 20 show an expanded view centered at the [100] direction and encompassing ±40°. The corresponding locations in elastic-parameter space for these selected images are noted in the two graphs in Fig. 21.

As in the positive-Δ regime, the ST slowness surface for negative-Δ materials arbitrarily close to the $\Delta=0$ line contains regions of saddle curvature around the ⟨111⟩ directions. For anisotropies between $\Delta=0$ and curve A, the saddle regions extend from the ⟨111⟩ directions partway toward adjacent ⟨100⟩ directions, as the slowness surface in Fig. 17(a) indicates. The resulting focusing pattern, seen in Fig. 18(a), appears qualitatively identical to those of the ST mode in positive-Δ materials close to the isotropy line. At curve A new areas of saddle curvature arise, originating at the ⟨100⟩ directions and stretching toward nearby ⟨111⟩ directions. Figures 17(b) and 18(b) show the slowness surface and intensity pattern for anisotropies slightly beyond A (point II in Fig. 21). Between curves A and B, the saddle regions merge together, forming a continuous furrow between adjacent ⟨100⟩ and ⟨111⟩ directions. This is the case for diamond (C), whose intensity pattern is shown in Fig. 18(c). The locus of points for which the two saddle regions have just merged is the dotted-dashed line labeled i in both graphs in Fig. 21.

As the anisotropy is increased further, the four ⟨100⟩ saddle lobes fuse together. In fact, as curve B is reached, a continuous region of the slowness surface around each ⟨100⟩ direction becomes saddle shaped. Figure 17(c) illustrates this situation. The corresponding Monte Carlo simulation in Fig. 19(a) reveals how this merging of the saddle lobes alters the ⟨100⟩ focusing structure. Instead of meeting at a point in the ⟨100⟩ directions, the fold caustics now overlap each other as they wrap around the symmetry direction.

The slowness surface shown in Fig. 17(d) is representative of the topology found in materials whose anisotropy lies beyond critical curve C. Small cloverleaves of concave curvature now appear inside the saddle region, centered at the ⟨100⟩ directions. Examination of Fig. 14 reveals that these areas are responsible for small ⟨100⟩-centered cusp structures in the focusing pattern. Monte Carlo simulations in Figs. 19(b) through 19(d) for points IV through VI show that this interior structure varies appreciably as the anisotropy changes between curves C and D. As the anisotropy changes, the cusp-fold caustic in each symmetry-reduced segment [line BDC in Fig. 14(c)] changes its orientation or tilt with respect to the {001} planes. The change is due to the gradual increase in size of the cloverleaves; as they expand, their parabolic lines approach the {001} planes, so that phonons on the caustics are focused closer to those planes.

As the anisotropy is increased past critical curve D, the cloverleaves merge into a single concave area around the

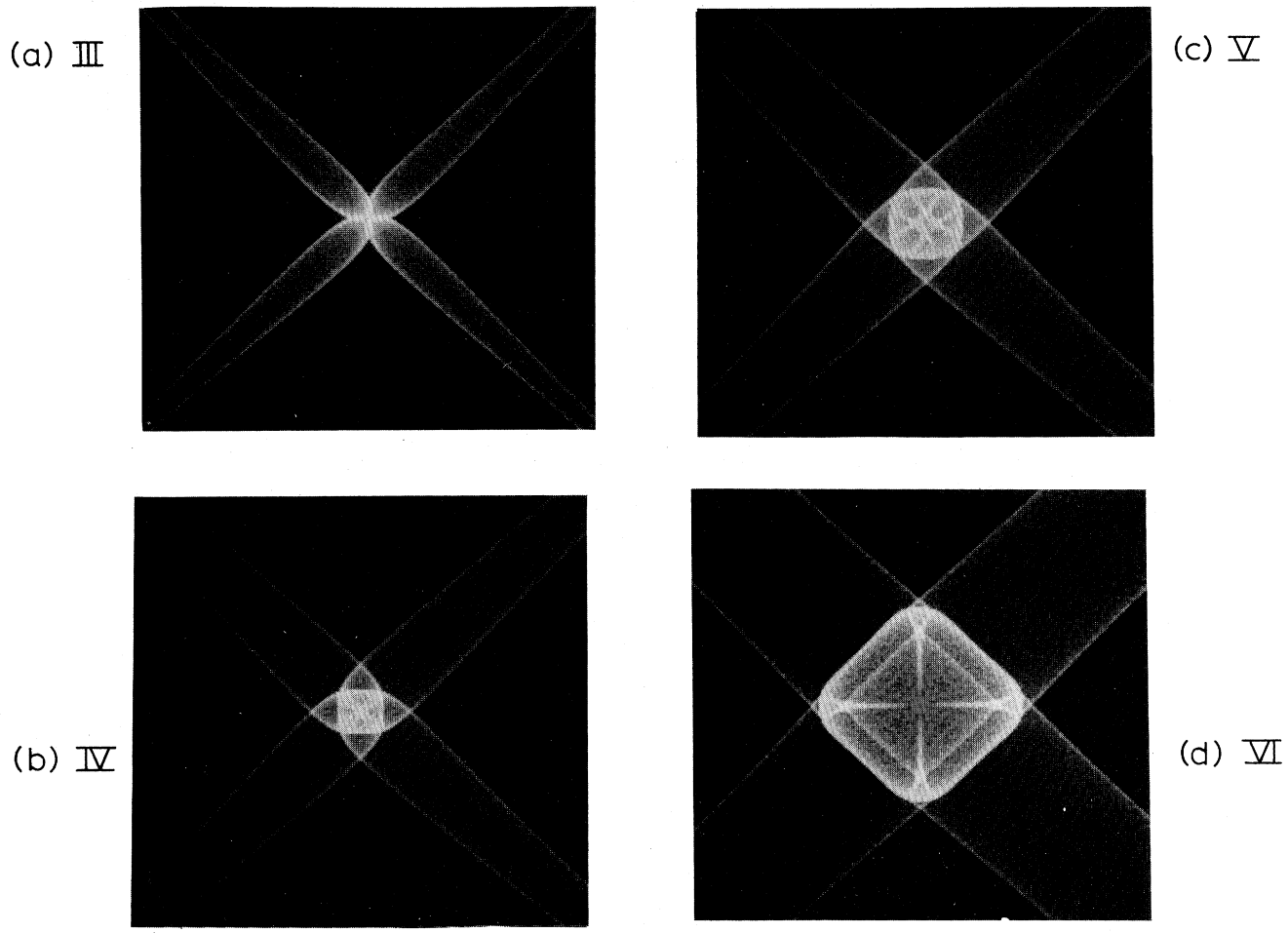

FIG. 19. ST-mode intensity-pattern simulations for several negative-Δ materials between critical curves B and D. These images are rotated 45° with respect to those in Fig. 18. The simulations are centered on the [100] direction and span ±20° left to right. Plotted in Fig. 21, the values chosen for a and b are as follows: (a) $a=2.275$, $b=0.725$ (point III); (b) $a=2.225$, $b=0.775$ (point IV); (c) $a=2.20$, $b=0.80$ (point V); and (d) $a=2.10$, $b=0.90$ (point VI).

$\langle 100 \rangle$ directions, as Fig. 17(e) indicates. The flux-intensity simulations of points VII and VIII in Figs. 20(a) and 20(c) and for copper (Cu) in Fig. 20(b) show the evolution of the focusing pattern for anisotropies beyond curve D. Formation of a single concave region around $\langle 100 \rangle$ means that the four separate inner caustics merge into one continuous caustic. As the concave region increases in size and curvature, this inner caustic moves away from the symmetry direction, until it touches the outer folds at the (001) and (010) planes (for Cu). For larger anisotropies, the caustic due to the concave regions actually appears outside of the saddle caustics in these planes [Fig. 20(c)]. (Examples of several types of catastrophes can be observed as the $\langle 100 \rangle$-centered caustic structure evolves. A discussion of this is in Ref. 15.) Figure 20(c) also reveals that as the anisotropy is increased, an enlargement of the entire focusing structure occurs, and the $\langle 111 \rangle$-centered cusps eventually move inside the $\langle 100 \rangle$-centered square structure.

A representative feature of the ST-mode focusing pattern is the "ramp," or pair of fold caustics that extends from near a $\langle 100 \rangle$ direction toward a $\langle 111 \rangle$ direction, where they meet with other caustic pairs to form the three-cusped structure. The separation of the cusps from $\langle 111 \rangle$ indicates the width of the ramp. As shown in Fig. 21(a), we define α_{1-} as the angle between one of the three cusps and the [111] direction. The dashed curves in Fig. 21(b) are curves of constant α_{1-}.

Another prominent feature in the ST-mode pattern is the bright square centered about the $\langle 100 \rangle$ directions [e.g., Fig. 20(a)]. This structure actually consists of overlapping V-shaped folds which form the boundaries of the ramps. With increasing anisotropy, the "square" changes size, shape, and orientation. Let β_{1-} be the angle between the [100] direction and intersection of the square with the (001) plane, as shown in Fig. 21(a). Figure 21(c) shows the curves of constant β_{1-}.

Thus, the focusing structures for materials with negative Δ are most complicated near the $\langle 100 \rangle$ crystalline directions. Intense FT ridges occupy the $\{100\}$ planes.

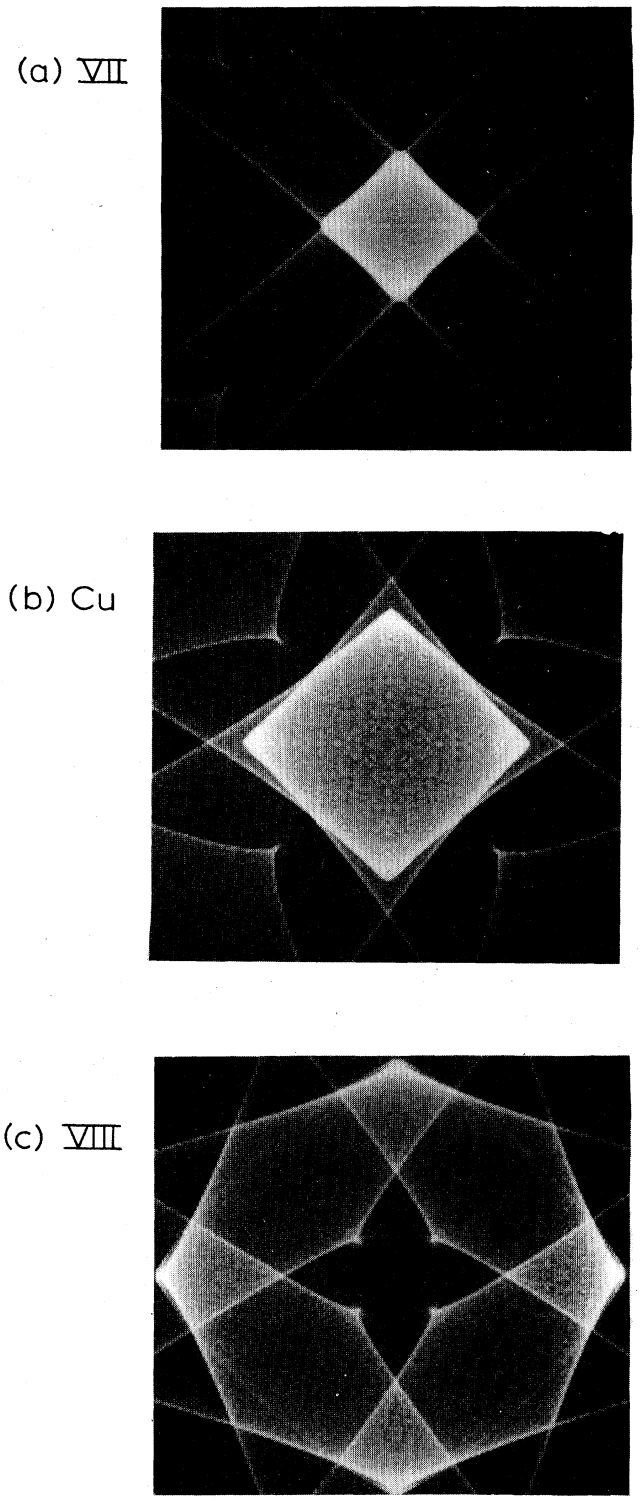

FIG. 20. Monte Carlo simulations of the ST focusing pattern for negative-Δ crystals located beyond critical curve D. In creating the simulations, the following pairs of a and b were used: (a) $a=2.00$, $b=1.00$ (point VII in Fig. 21); (b) $a=2.23$, $b=1.61$ (Cu); and (c) $a=1.60$, $b=1.40$ (point VIII). The simulations are centered on the [100] direction and represent a scan of $\pm 40°$ left to right.

Ramps in the ST focusing pattern reach between ⟨100⟩ and adjacent ⟨111⟩ directions, and additional cusped structures occur near the ⟨100⟩ directions. The dimensions of the FT ridge caustics can be described with one angle, and the principal changes that occur in the ST-mode caustics can be approximately characterized with the use of two angles.

V. SUMMARY

The phonon-focusing patterns associated with low-temperature heat-pulse propagation in cubic crystals has been systematically described. Depending on the values of the elastic constant ratios $a=C_{11}/C_{44}$ and $b=C_{12}/C_{44}$, a material can be assigned to one of two classes, determined by the sign of the parameter $\Delta \equiv a-b-2$, where isotropy corresponds to $\Delta=0$. Qualitative differences are observed between the phonon-focusing patterns of positive- and negative-Δ crystals. To provide specific examples of the focusing features typical of each regime, the slowness and wave surfaces of CaF_2 and Si were examined in detail.

The qualitative changes that take place in the focusing pattern as the elastic ratios are hypothetically varied have been investigated by studying (a) the evolution in the slowness-surface topology and (b) the corresponding changes in Monte Carlo flux-intensity simulations. Intensity patterns for nearly isotropic materials show little or no singular focusing. As the anisotropy is increased, the angular size and complexity of the singular structures increase.

In general, a quantitative prediction of the anisotropy in phonon flux requires a detailed Monte Carlo calculation. However, the angular dimensions of the principal caustics can be described by a small number of angles. We have defined a set of such angles and determined their variation in the elastic-parameter space. Using this information (Figs. 9, 12, 16, and 21), the singularity pattern for a cubic crystal of arbitrary elastic constants can be easily predicted.

ACKNOWLEDGMENTS

The computer programs used to generate the slowness surfaces and group-velocity surfaces were developed by G. A. Northrop, as were the subroutines on which the flux-intensity simulation program is based. We also appreciate the expertise and enthusiasm of A. G. Every, and his discussions on the mathematical aspects of phonon focusing. This work was supported by the National Science Foundation under the Materials Research Laboratory Grant No. DMR 83-16981.

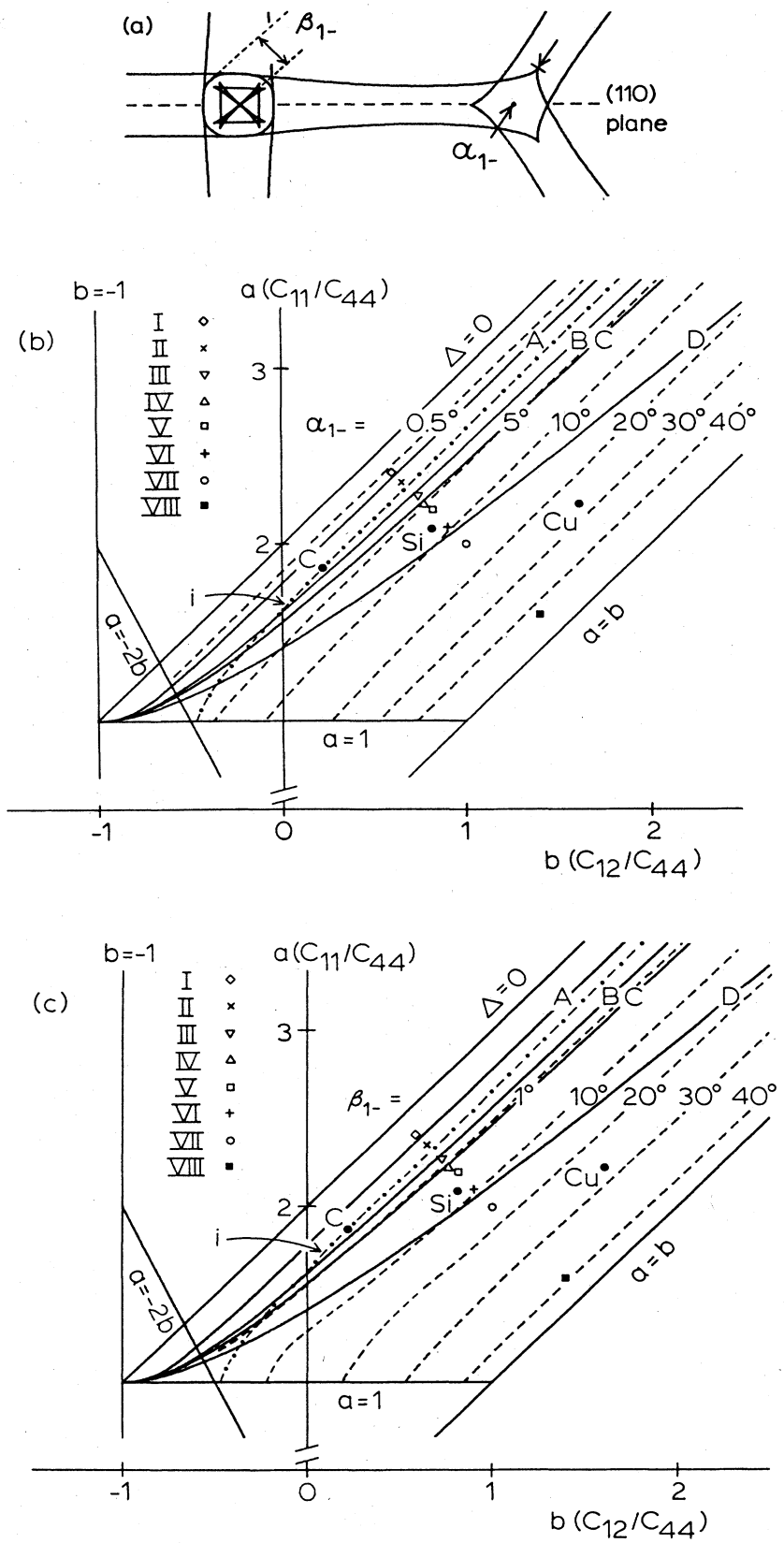

FIG. 21. Angular dimensions that describe the negative-Δ ST focusing pattern. (a) Singularity map showing the definitions of angles α_{1-} and β_{1-}. (b) Lines for which α_{1-} is a constant. (b) Curves for various values of β_{1-}. The dashed-dotted curve labeled i in both graphs indicates the locus of points for which the ⟨100⟩ and ⟨111⟩ saddle regions have just merged.

[1]H. J. Maris, J. Acoust. Soc. Am. **50**, 812 (1971).
[2]F. Rösch and O. Weis, Z. Phys. B **25**, 101 (1976).
[3]G. A. Northrop and J. P. Wolfe, Phys. Rev. B **22**, 6196 (1980).
[4]J. C. Hensel and R. C. Dynes, Phys. Rev. Lett. **39**, 969 (1977); **43**, 1033 (1979); in *Proceedings of the 14th International Conference on the Physics of Semiconductors, Edinburgh, 1978,* edited by B. L. H. Wilson (IOP, London, 1978), p. 371.
[5]M. Greenstein and J. P. Wolfe, Phys. Rev. Lett. **41**, 715 (1978); Phys. Rev. B **24**, 3318 (1981).
[6]M. Greenstein, M. A. Tamor, and J. P. Wolfe, Phys. Rev. B **26**, 5604 (1982).
[7]M. A. Tamor, M. Greenstein, and J. P. Wolfe, Phys. Rev. B **27**, 7353 (1983).
[8]S. J. Kirch and J. P. Wolfe, Phys. Rev. B **29**, 3382 (1984).
[9]G. A. Northrop, E. J. Cotts, A. C. Anderson, and J. P. Wolfe, Phys. Rev. Lett. **49**, 54 (1982); Phys. Rev. B **27**, 6395 (1983).
[10]G. L. Koos and J. P. Wolfe, Phys. Rev. B **29**, 5 (1984); **30**, 3470 (1984).
[11]W. Dietsche, G. A. Northrop, and J. P. Wolfe, Phys. Rev. Lett. **47**, 660 (1981).
[12]S. Tamura, Phys. Rev. B **25**, 1415 (1982); **28**, 897 (1983).
[13]J. P. Wolfe and G. A. Northrop, in *Proceedings of the Fourth International Conference on Phonon Scattering in Condensed Matter, Stuttgart, 1983,* edited by W. Eisenmenger, K. Lassmann, and S. Döttinger (Springer, New York, 1984), p. 100.
[14]S. Tamura, Phys. Rev. B **30**, 849 (1984).
[15]A. G. Every, Phys. Rev. B **24**, 3456 (1981).
[16]D. Armbruster and G. Dangelmayr, Z. Phys. B **52**, 87 (1983).
[17]M. J. P. Musgrave, *Crystal Acoustics* (Holden-Day, San Francisco, 1970).
[18]F. I. Fedorov, *Theory of Elastic Waves in Crystals* (Plenum, New York, 1968).
[19]See, for example, B. A. Auld, *Acoustic Fields and Waves in Solids* (Wiley, New York, 1973), Vol. 1.
[20]Values taken from G. Simmons and H. Wang, *Single Crystal Elastic Constants and Calculated Aggregate Properties* (MIT, Cambridge, Mass., 1971). Low-temperature (<4-K) values were used if available.
[21]J. F. Nye, *Physical Properties of Crystals* (Oxford University Press, London, 1957).
[22]J. C. Hensel and R. C. Dynes, Phys. Rev. Lett. **43**, 1033 (1979).
[23]M. Lax and V. Narayanamurti, Phys. Rev. B **22**, 1746 (1980).
[24]G. F. Miller and M. J. P. Musgrave, Proc. R. Soc. London, Ser. A **236**, 352 (1956).
[25]E. B. Christoffel, Ann. Mat. Pura Appl. **8**, 193 (1877); see also A. G. Every, Phys. Rev. Lett. **42**, 1065 (1979); Phys. Rev. B **22**, 1746 (1980).
[26]M. J. P. Musgrave, Proc. Cambridge Philos. Soc. **53**, 897 (1957).
[27]M. J. P. Musgrave, J. Elast. **9**, 105 (1979).
[28]S. R. Prabhakaran and K. S. Viswanathan, Can. J. Phys. **50**, 1903 (1972).
[29]G. F. D. Duff, Philos. Trans. R. Soc. London **252**, 249 (1960).

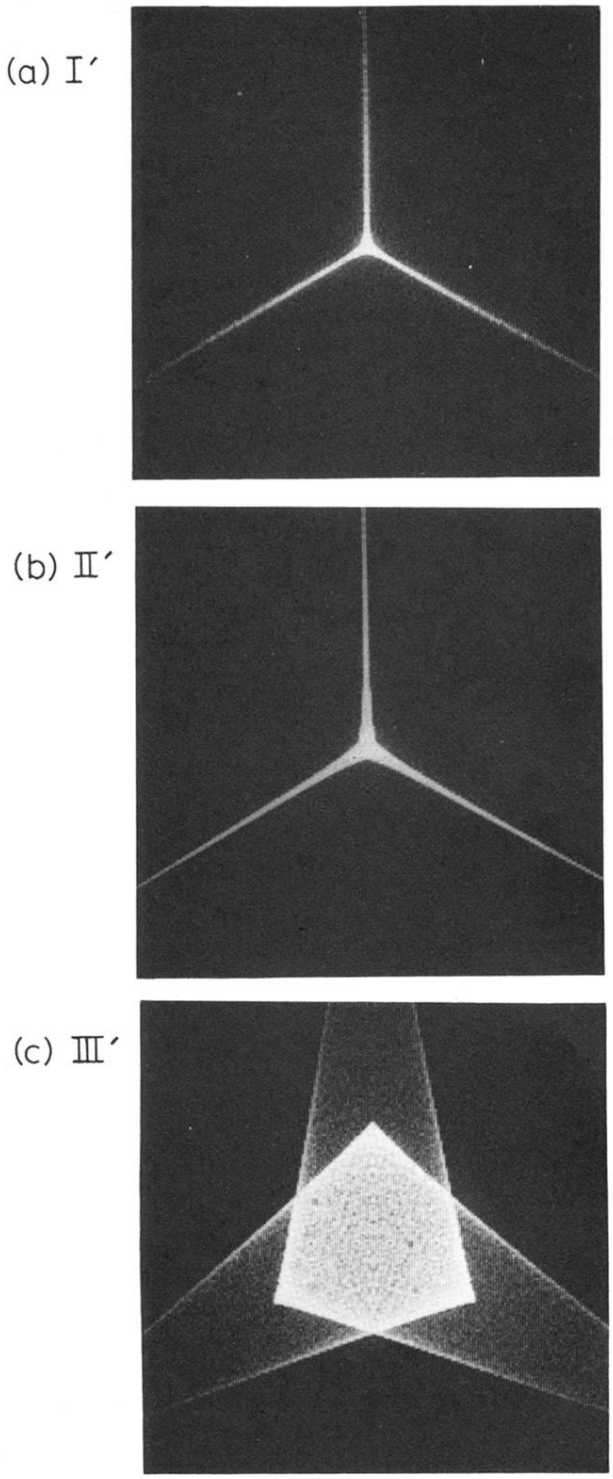

FIG. 11. ST-mode Monte Carlo simulations corresponding to the slowness surfaces in Fig. 10. The simulations are centered on the [111] direction and span ±35° left to right.

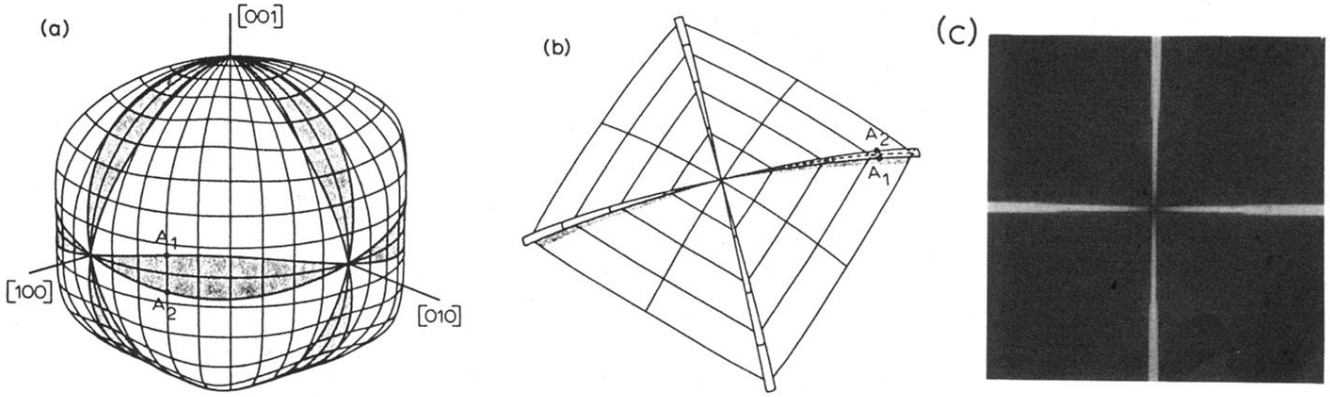

FIG. 13. (a) FT slowness surface for Si. Points A_1 and A_2 map into points A_1 and A_2 on the group-velocity surface in (b). (b) Section of the FT-mode group-velocity surface near the [100] direction. (c) FT-mode flux-intensity simulation for Si, centered on the [100] direction and covering a scan of $\pm 45°$.

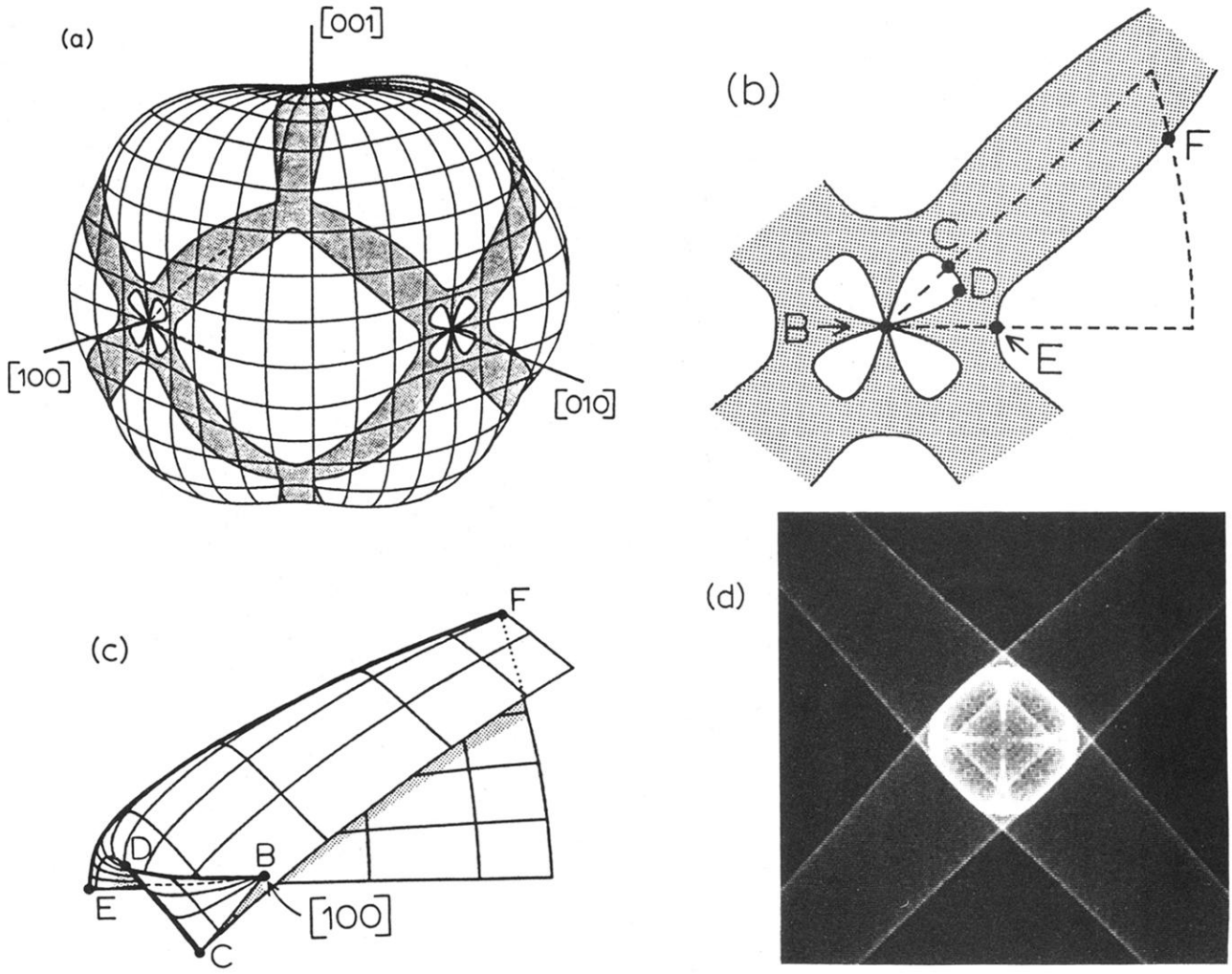

FIG. 14. (a) ST slowness surface for Si. The small cloverleaf sections of the surface surrounding each ⟨100⟩ direction are concave in curvature. (b) Symmetry-reduced portion of the ST slowness surface near [100]. The part of the surface enclosed by dashed lines maps into the portion of the group-velocity surface shown in (c). (c) Symmetry-reduced segment of the ST group-velocity surface for Si near the [100] crystalline direction. The remainder of the surface can be obtained by reflecting in (100) and (110) planes. (d) ST-mode flux-intensity simulation for Si, centered on the [100] direction and spanning ±20° left to right.

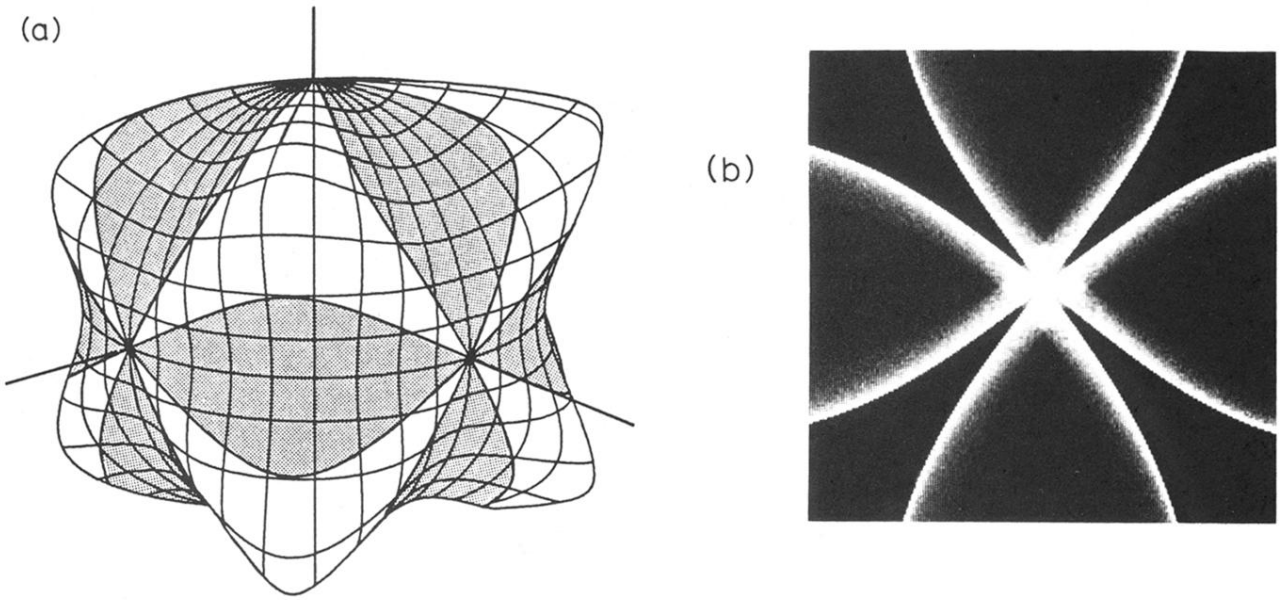

FIG. 15. (a) FT slowness surface for the point $a = 1.60$, $b = 1.40$ (negative-Δ regime). (b) Corresponding Monte Carlo simulation for FT phonons, centered on the [100] direction and spanning $\pm 45°$ left to right.

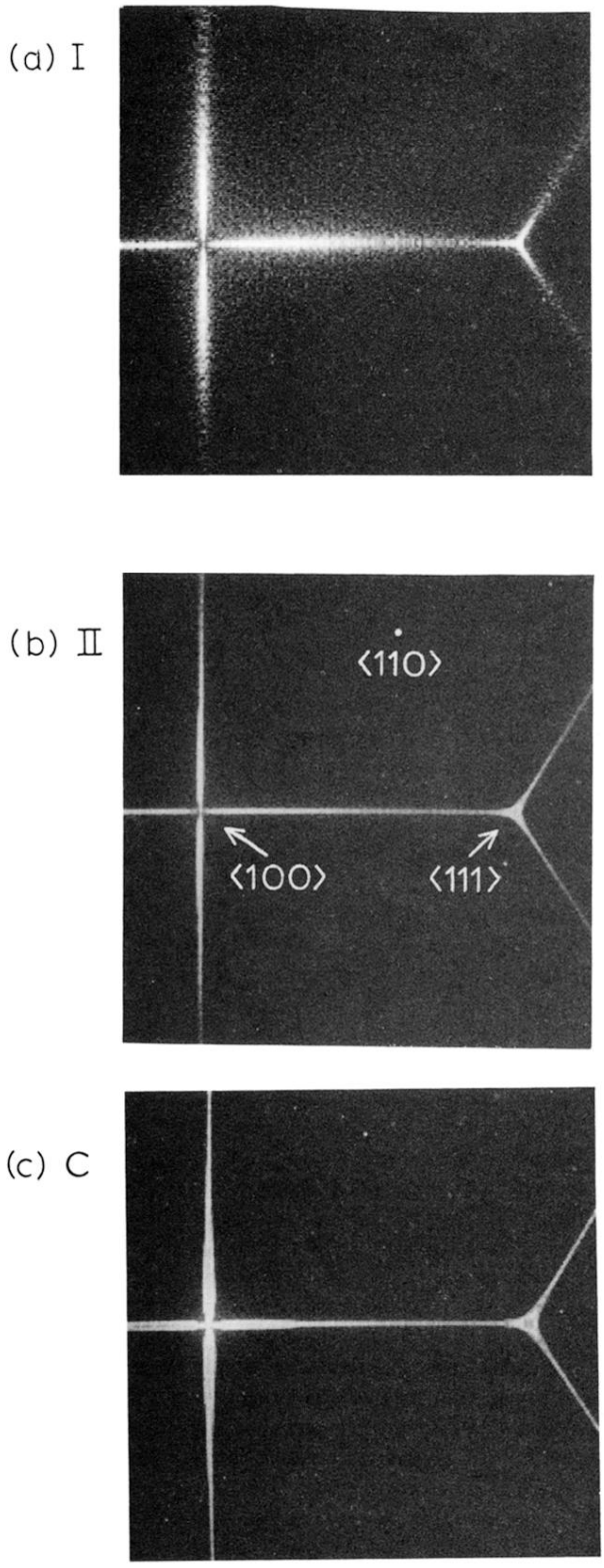

FIG. 18. ST-mode flux-intensity simulations for several negative-Δ elastic ratios. The elastic ratios used for the simulations have anisotropies between $\Delta=0$ and critical curve C, as shown in Fig. 21. The following elastic ratios were used: (a) $a=2.40$, $b=0.60$ (point I); (b) $a=2.35$, $b=0.65$ (point II); and (c) $a=1.87$, $b=0.22$ (diamond, C). The simulations are centered on the $[2\sqrt{2},1,1]$ crystalline direction and represent a scan of $\pm 38°$ left to right.

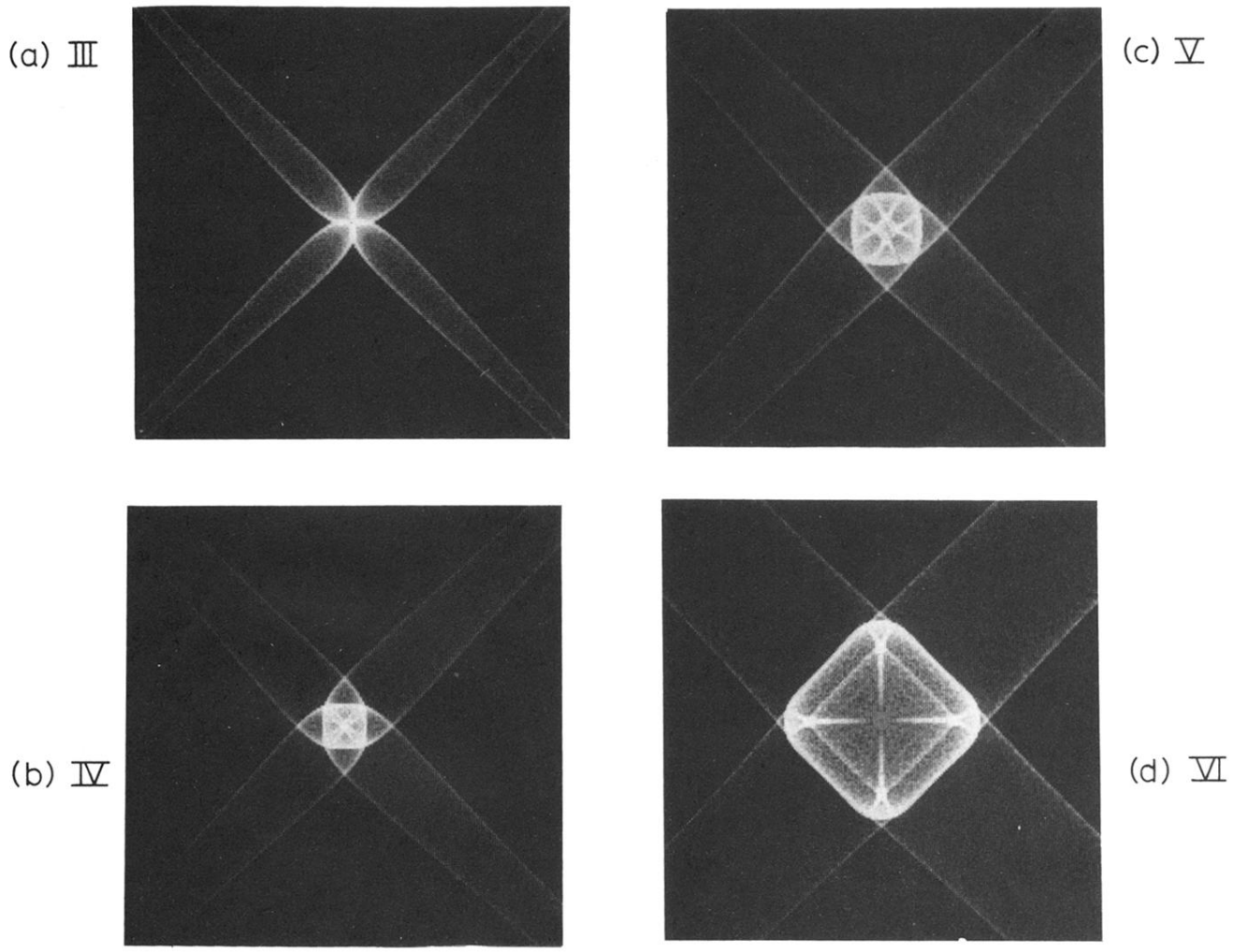

FIG. 19. ST-mode intensity-pattern simulations for several negative-Δ materials between critical curves B and D. These images are rotated 45° with respect to those in Fig. 18. The simulations are centered on the [100] direction and span ±20° left to right. Plotted in Fig. 21, the values chosen for a and b are as follows: (a) $a=2.275$, $b=0.725$ (point III); (b) $a=2.225$, $b=0.775$ (point IV); (c) $a=2.20$, $b=0.80$ (point V); and (d) $a=2.10$, $b=0.90$ (point VI).

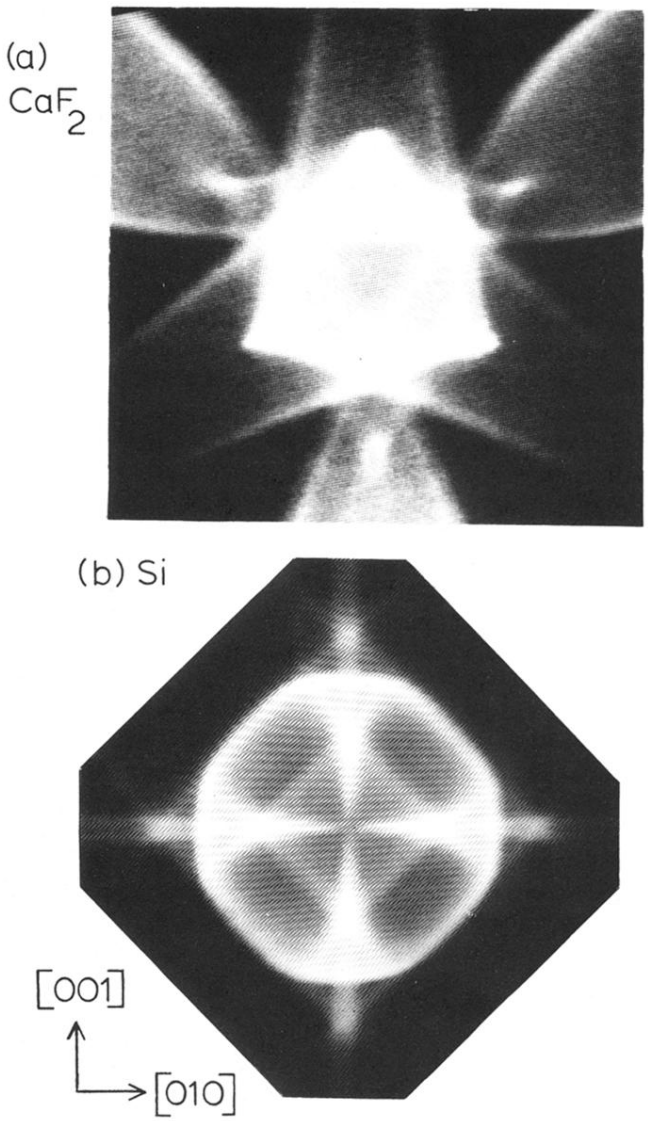

FIG. 2. (a) Experimental heat-pulse image for CaF_2, centered on the [111] direction. The image spans ±23° left to right. (b) Phonon image for Si, centered on the [100] direction and spanning ±12°. These phonon images were recorded using a broad time gate so that both transverse phonon modes were included.

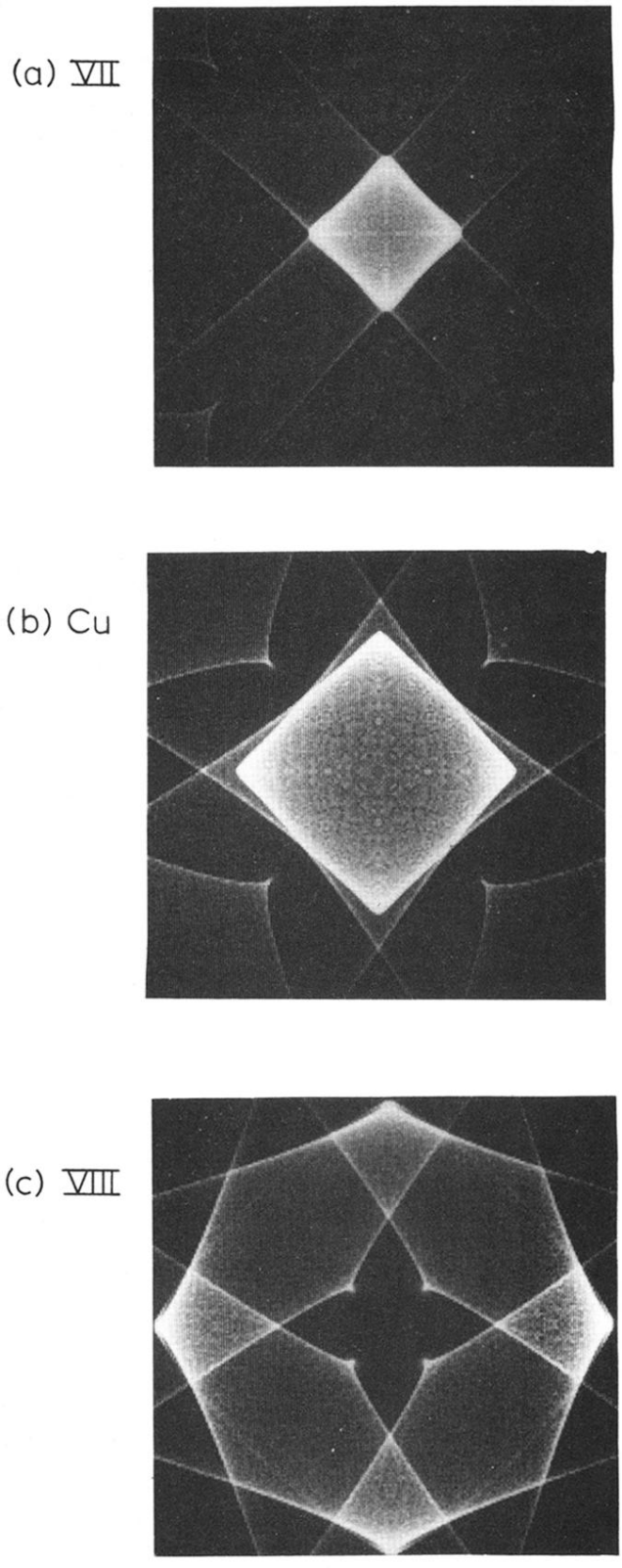

FIG. 20. Monte Carlo simulations of the ST focusing pattern for negative-Δ crystals located beyond critical curve D. In creating the simulations, the following pairs of a and b were used: (a) $a=2.00$, $b=1.00$ (point VII in Fig. 21); (b) $a=2.23$, $b=1.61$ (Cu); and (c) $a=1.60$, $b=1.40$ (point VIII). The simulations are centered on the [100] direction and represent a scan of $\pm 40°$ left to right.

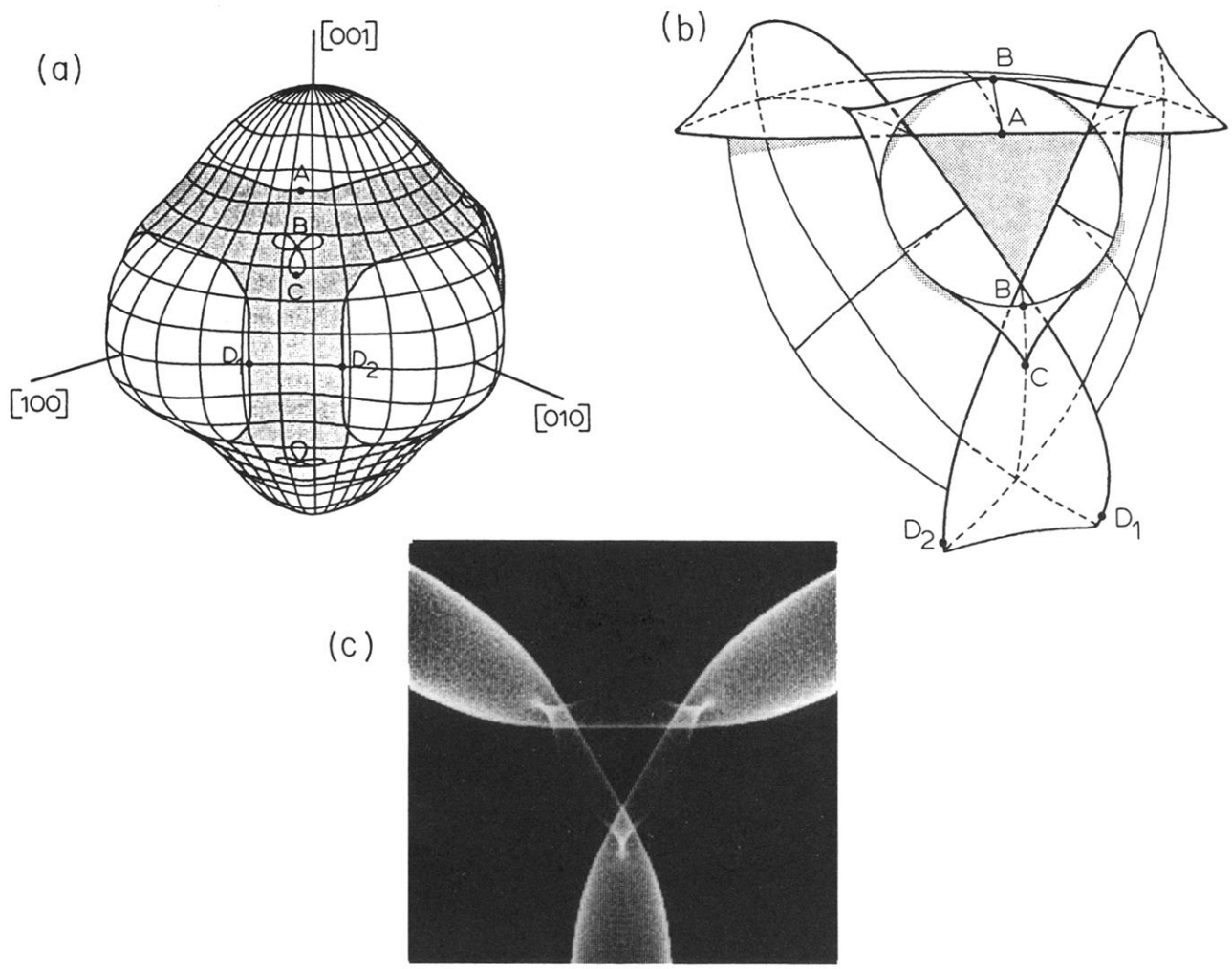

FIG. 5. (a) FT slowness surface for CaF_2. Phonons with **k** vectors at points *A* through *D* on this surface are focused into points *A* through *D* on the group-velocity surface in (b). Shading indicates areas of saddle (negative) curvature. All other portions of this surface are convex. Thick lines outlining saddle regions represent lines of zero Gaussian curvature and correspond to folds in the group-velocity surface. (b) Representation of the FT group-velocity surface near the [111] direction. No phonons are focused into the central shaded region. Thick lines represent folds which correspond to lines of mathematically infinite flux intensity (caustics). (c) Monte Carlo flux-intensity simulation for FT phonons in CaF_2. This image is centered on [111] and represents a scan of $\pm 35°$ from left to right.

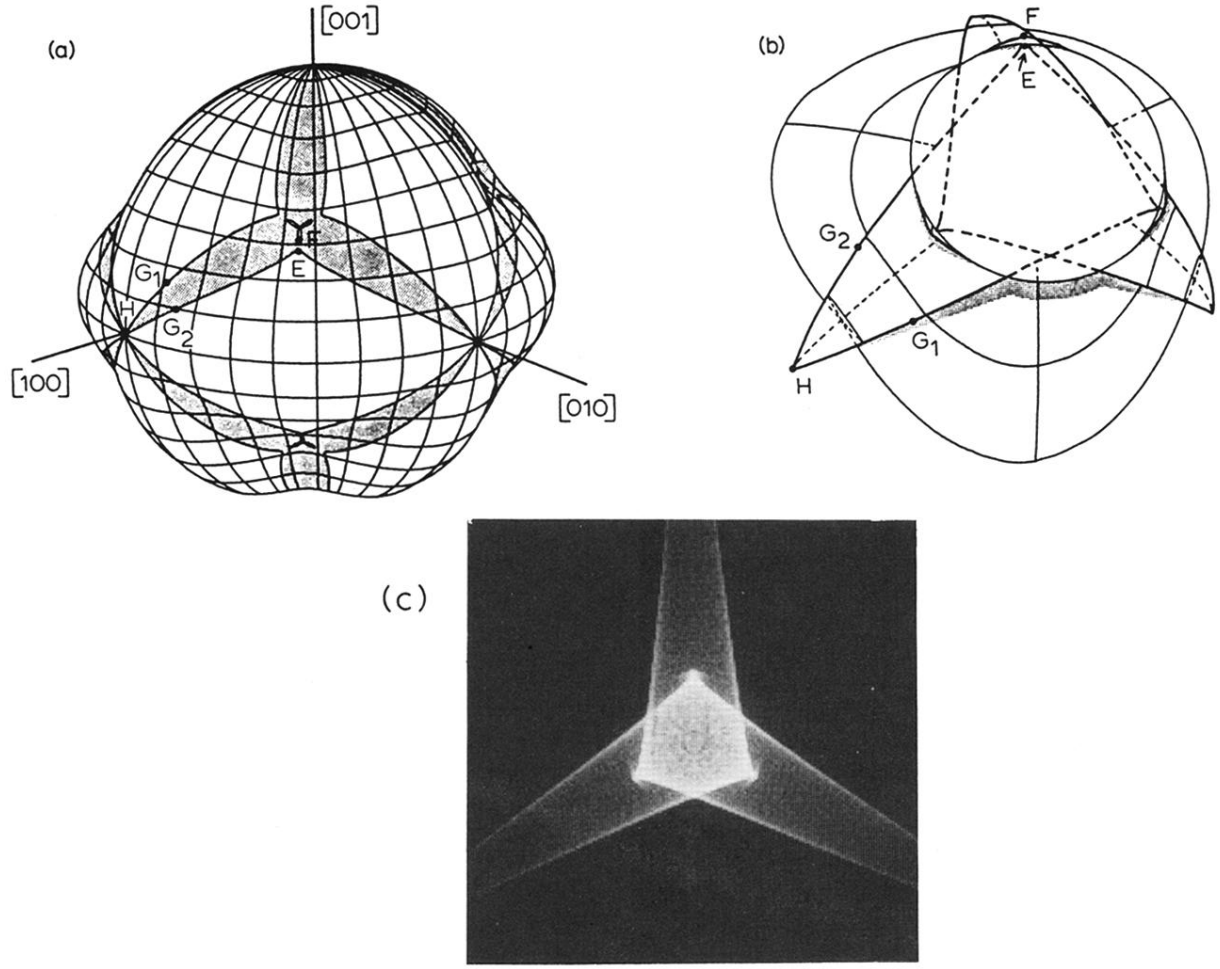

FIG. 6. (a) ST slowness surface for CaF_2. Points E through H on this surface correspond to points E through H on the velocity surface in (b). The three small areas forming the cloverleaf structure near $\langle 111 \rangle$ are concave. (b) Portion of the ST-mode group-velocity surface near the [111] direction. (c) Monte Carlo simulation for ST phonons. The image is centered on the [111] direction, and represents a scan of $\pm 35°$ left to right.

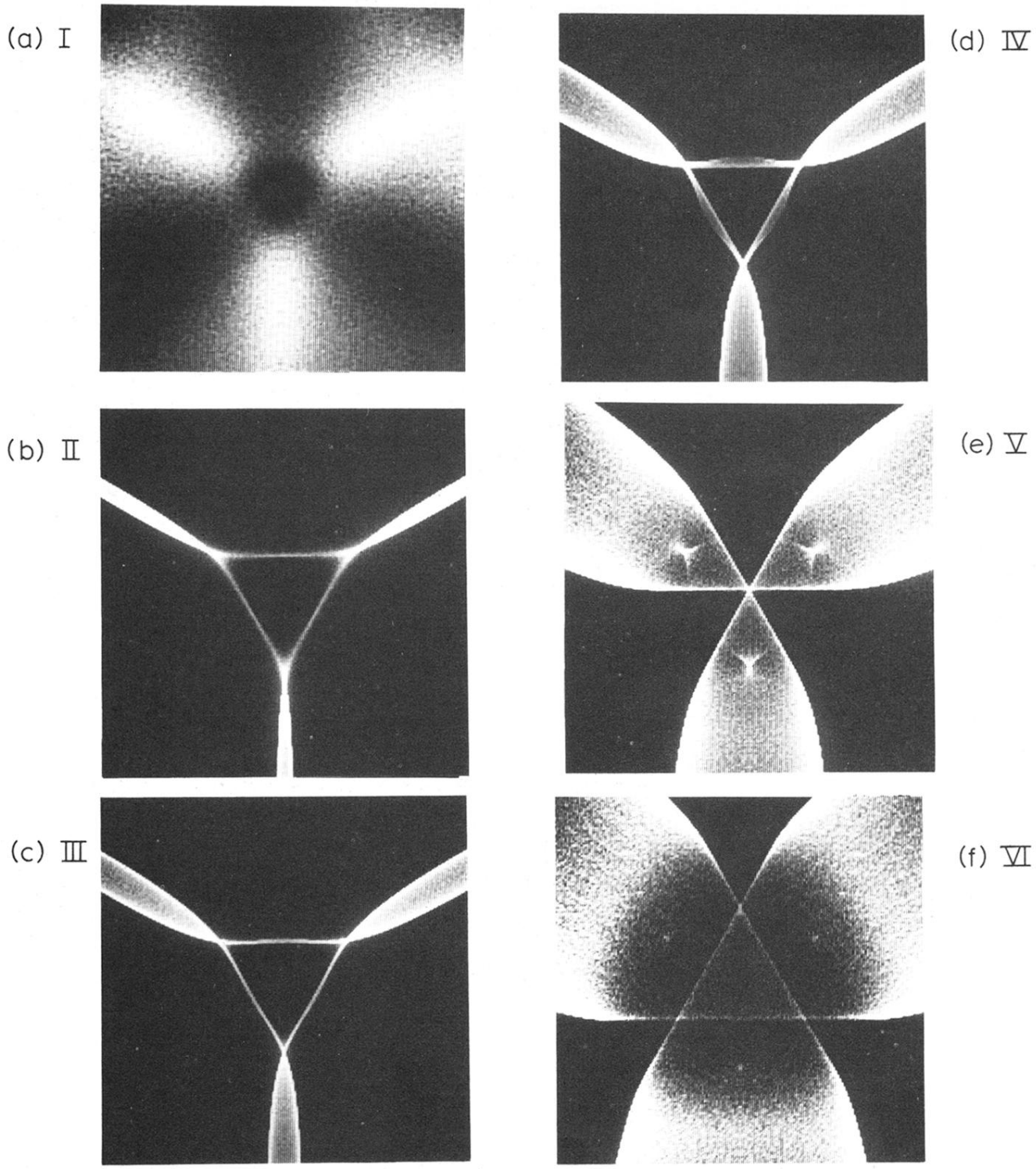

FIG. 8. FT-mode Monte Carlo simulations for values of a and b in the positive-Δ regime. Each simulation is centered on the [111] crystalline direction and spans $\pm 35°$ left to right, so that the [110] direction lies at the center of the lower edge of the images. The combinations of a and b used in the simulations are labeled as points in Fig. 9. The simulations were calculated with the following values: (a) $a=2.95$, $b=0.65$ (point I in Fig. 9); (b) $a=3.15$, $b=0.47$ (point II); (c) $a=3.20$, $b=0.40$ (point III); (d) $a=3.25$, $b=0.35$ (point IV); (e) $a=3.54$, $b=0.00$ (point V); and (f) $a=3.75$, $b=-0.50$ (point VI).